Experimental and numerical investigation of a porous receiver equipped with Raschig Rings for CSP applications

Experimental and numerical investigation of a porous receiver equipped with Raschig Rings for CSP applications

Laura Savoldi [1]*, Andrea Allio [1], Antonio Bonvento [1], Marco Cantone [1], Jesus Fernandez Reche [2]

[1] Dipartimento Energia "Galileo Ferraris", Politecnico di Torino, Torino (Italy);
[2] CIEMAT, Plataforma Solar de Almería, Tabernas-Almería (Spain)

* Corresponding author: laura.savoldi@polito.it; Tel.: +39 011 090 4559

Abstract: In the context of central solar tower systems, tubular receivers are among the most appealing absorber solutions: the absorbed solar radiation is transferred from the tube external surface to the heat transfer fluid (HTF) flowing within the absorber. In the case of air as HTF, very high temperatures of the coolant can be obtained in principle, thus increasing the efficiency of the downstream thermodynamic cycle. To explore the possible applicability of a porous medium made of Raschig Rings (RRs), already successfully adopted in the heat removal from the resonant cavity of a technological device, the gyrotron, where the heat flux can go up to 20-25 MW/m^2 and removed by subcooled water, a mock-up of a planar receiver equipped with RRs has been tested in a solar furnace, using air as coolant. The test results are presented here and analyzed[1]. Furthermore, a numerical model of the mock-up, where the RRs are modeled in detail by the Discrete Element Method, is presented and its capability to reproduce the measured data demonstrated. The model shows, for the tested configuration, an enhancement of the heat transfer of a factor of ~ 5 with respect to a plain channel with the same envelope, and a Performance Evaluation Criteria of 2-2.5 when the device is compared to the same receiver configuration, but without RRs.

Keywords: CSP, Tubular receiver, CFD, Raschig Rings, Porous matrix, DEM

1. Introduction

In the context of concentrated solar power (CSP), tubular receivers for central solar tower systems can largely benefit from the use of porous matrices to enhance the heat transfer to the coolant. This paper focuses on the analysis of a porous medium never investigated so far for solar applications, i.e. the Raschig Rings, originally invented and developed for packed-bed reactors (Sella, 2008) and adopted in the removal of high heat fluxes in niche applications in the Nuclear Fusion field, namely the gyrotron resonant cavity.

CSP technologies use different mirror configurations to concentrate the sunlight energy onto a receiver and convert it into heat. The sun's rays are used to heat a medium, usually a fluid or a gas, that is then used in a heat engine process (steam or gas turbine) to drive an electrical generator and produce electricity or used as industrial process heat. CSP uses only the beam component of solar radiation (direct normal irradiance), and so its maximum benefit tends to be restricted to a limited geographical range (European Commission, 2019). Among the CSP systems, Solar Central Tower, with their single receiver placed on top of a tower surrounded by many heliostats and very high concentration ratios, can reach higher temperatures and greater thermodynamic cycle efficiency than other systems. This technology can produce utility-scale electricity, offering dispatchable power on demand by integrating thermal energy storage.

[1] Based on experiments carried out at the Plataforma Solar de Almeria

In the context of solar towers, tubular receivers are probably the most appealing absorber solutions (Conroy et al., 2019). At the commercial level, tubular receivers adopt liquid heat transfer fluid, like water and molten salts; however, they can easily work also with pressurized gases, as demonstrated for example in the SOLHYCO project (European Commission, 2011). The use of a gaseous working fluid (typically pressurized air) could improve effectively the tubular receiver performance since the gas has no upper temperature limit by itself, whereas the limit is set by the thermo-mechanics of the pipes. In addition, when air is used as a working fluid, a gas turbine could be directly driven by the solar field, allowing the implementation of a solar-driven combined cycle. The advantages of air, however, are counterbalanced by the lower heat transfer coefficient (HTC) with respect to liquids, which leads to higher temperatures of the tube wall and consequently higher thermal stresses, which limit the applicable solar incident heat flux on the absorber surface. At the same time, the wetted surface to transfer a given thermal power needs to be increased to compensate for the low HTC, if the same temperature of liquid coolant is targeted at the outlet of the receiver.

The enhancement of the convective heat transfer between the tube wall and the coolant could help reducing the peak temperature. That target can be achieved then by increasing the HTC or by increasing the heat transfer surface, or both.

The first option was already explored in several studies, both experimentally and numerically, investigating different possible alternatives. In the above mentioned SOLHYCO project (European Commission, 2011), developed in 2006-2010 at the Plataforma Solar de Almeria, a profiled multilayer tube receiver was demonstrated to enhance the heat transfer from the irradiated tube wall to the gas and to reduce the temperature difference over the circumference of the tube. Tubes with an enhanced heat transfer obtained through internal periodic ribs were experimentally investigated in (Yang et al., 2010), using molten salt as cooling fluid, under a uniform heat flux to the pipe obtained using an electric heater, demonstrating that the heat transfer of the tube equipped with helical ribs was three times higher than that of the corresponding smooth pipe. In (Uhlig et al., 2015), corrugated tubes equipped with helical ribs were analyzed numerically, without any experimental validation, demonstrating that helical ribs reduce both the maximum and the average tube wall temperature. In (Cantone et al, 2020), 3D-printed Inconel® tubes equipped with helical ribs or annular rings were manufactured and tested within the SFERA II project at the Plataforma Solar de Almeria as solar tubular receivers. The experimental and numerical (CFD) investigation of the one-side heated tubes led to the conclusion that turbulence promoters allow reducing the thermal gradients between the irradiated and the non-irradiated (back) side of the tube.

A way of enhancing the convective heat transfer from the wall to the fluid, alternative to any attempt to increase directly the HTC, is to insert a porous medium under the irradiated surface. Porous media are widely applied in industry to enhance the heat transfer rate from catalyst carriers in chemistry, thermal exchange in electrical cooling, thermal insulation in buildings and astronautics, low emission combustion technologies and receivers for concentrating solar power. The adoption of porous media typically increases the useful heat transfer surface: a reduction of both convective and radiative heat losses is expected, as well as the thermal stresses of the tube.

In the CSP field, porous media could be adopted either into the pipes of tubular receivers or as receivers themselves. In the first case, it is easy to compare the performance to that of a "plain" tubular receiver: the maximum applicable solar incident heat flux on the absorber surface could be increased or the absorber area could be reduced for the same incident solar power, typically at the cost of increased pressure drop across the tube. If the porous medium itself is adopted as a receiver, we face a "volumetric receiver", which is a thermal system where the concentrated radiation is absorbed directly on the surface of a (porous) material, that transfers heat to a working fluid (typically air). Different materials and shapes (ceramic structure of silicon carbide honeycomb (Hoffschimdt et al., 1999), (Hoffschimdt et al., 2003), foams made out of aluminum oxide, coated with black paint to increase the solar absorption (Skocypec et al., 1989) were designed and tested, reaching outlet temperatures up to 700°C - 800°C (Hoffschimdt et al., 2003). Several numerical investigations were also carried out on the volumetric receivers, focusing both on flow/pressure drop, see for instance (Becker et al., 2006) and (Wu et al., 2010) and heat transfer, as in (Zhu et Xuan, 2018)). In (Cagnoli et

al., 2019), a coupled CFD and optical analysis allowed identifying the best configuration (e.g., pore size) to maximize the receiver efficiency.

Considering the convective heat transfer enhancement obtained by porous media inserted *into* tubular receivers, tests and analyses have been performed by different authors considering tubes totally or partially filled by a porous matrix. Kumar (Kumar et al, 2009) presented a numerical analysis of porous disc receiver for solar parabolic trough collectors, concluding from simulations that the insertion of a porous medium in tubular solar receiver enhances the system performance significantly (~64.3% in terms of Nusselt number Nu) with respect to the same tubular receiver in the smooth configuration. Lim (Lim et al, 2014) performed a design optimization of a solar tubular receiver filled with a metal foam, considering length, porosity and thermal conductivity of the metal matrix as design factors. The authors of (Mwesigye et al., 2014) numerically investigated the thermal and thermodynamic performance of a tubular receiver with perforated plate inserts for a parabolic trough solar collector, with fixed porosity equal to 0.65. It was shown that the receiver temperature gradients reduced significantly with the use of inserts; correlations for Nu and the friction factor f were also derived from the numerical database. In (Zheng et al., 2017), the authors investigated a tubular receiver, cooled with molten salts, partially filled with a metal foam matrix under a non-uniform heat flux distribution. The optimized design resulted from a trade-off between improved heat transfer and increased pressure drop, showing that the enhanced receiver tube (ERT) with down-filling porous inserts (i.e., the porous medium fills only half of the cross-section, where the heat flux is hitting the pipe) and in-filling porous inserts (i.e., the porous medium fills only an inner circle of the pipe) has good thermal performance when the ratio of thermal conductivity of porous medium to working fluid is less than 1000. In (Alkam et Al-Nimr, 1997) the authors numerically investigated the problem of transient forced convection flow in a concentric annulus partially filled with porous substrates located either on the inner or the outer cylinder. An increase of up to 12 times in Nu was reported in comparison with the clear annuli case and the superiority in thermal performance of the case when the porous substrate was emplaced to the inner cylinder was outlined. Based on those results, in (Alkam et Al-Nimr, 1999) further investigations were carried out on the thermal performance of a conventional concentric-tube heat exchanger by emplacing porous substrates on both sides of the inner cylinder. Their numerical results showed that porous substrates of optimum thickness leads to the maximum improvement in the heat exchanger performance with a moderate increase in the pumping power. More recently, Mohamad (Mohamad, 2003) numerically investigated the heat transfer augmentation for flow in a pipe or a channel partially or fully filled with porous material emplaced at the core of the channel. It was shown that partially filling the channel with porous substrates can reduce the thermal entrance length by 50% and increase the rate of heat transfer from the walls.

In this study, the adoption of Raschig Rings (RR) (Sella, 2008) is investigated for the first time, both experimentally and numerically, in applications within tubular receivers in the CSP field. A receiver mock-up equipped with RRs, formerly used to assess thermal-hydraulic performance in a forced flow of water for heat flux conditions in the range 10-30 MW/m^2 (Rozier, 2015), has been tested at the Plataforma Solar de Almeria (PSA) in 2019, under different heat load and flow rate conditions using pressurized air as a cooling fluid, in the framework of the SFERA III European Project.

Thermal experimental tests (as opposed to hydraulic tests, see (Allio et al., 2020)) on devices equipped with RRs are not extensively documented in the literature, neither in the applications related to the packed-bed reactors nor in those related to gyrotrons and their resonator cavity cooling. Some numerical works have been performed in the past on RRs but related to other fields. Moghaddam and coauthors (Moghaddam et al., 2020) studied the *hydrodynamics* of random packings of RRs using the Rigid Body Dynamics (RBD) method and CFD simulations, demonstrating that the ring orientation largely influences the velocity distribution, and greater azimuthal and axial inhomogeneities occur with respect to spherical and cylindrical packings. In (Allio et al., 2020), an alternative model, based on the generation of a random distribution of RR using the Discrete Element Method (DEM) technique has been developed and validated against experimental results against pure hydraulic experimental data. As far as the thermal aspects are concerned, Dong and coauthors (Dong et al., 2017) improved innovative experimental techniques for high-quality temperature

measurement to validate DEM-CFD simulations of heat transfer in a fixed-bed reactor for both spherical and RRs packings in moderate flow conditions and high-temperature ranges. There, the model of *pure heat conduction* in the solid, subject to *uniform* heat flux, was proven to be correct. Marek (Marek, 2017) carried out a numerical study of *laminar* gas flow in a real geometry of a random packed bed of RRs, showing a good agreement with empirical correlations where pressure drop is expressed as a function of the gas velocity. No modeling of turbulent flow or conjugate heat transfer is found in the published literature. We address here for the first time the modeling and validation against experimental data of the conjugate heat transfer problem in a turbulent fluid flow within a RR matrix.

After describing the sample, the test setup and presenting the hydraulic and thermal-hydraulic test results obtained during the test campaign at PSA, we develop a suitable computational fluid dynamic (CFD) model for the receiver mock-up, where the RR geometrical random distribution is based on the DEM already used in (Allio et al., 2020). Even if the DEM strategy has been widely used in solar projects, particularly for solar particle receivers, where solid particles are used as the heat transfer medium, see (Zanino et al, 2016) and (Ho et al., 2017), this is the first time, to the best of our knowledge, that the DEM is applied to generate the model of a porous media inside a receiver, following what has already been done for the modeling of packed-beds and gyrotron resonators. The validation of the model against the experimental data collected during the experimental campaign at the PSA provides, within the error-bar, added value with respect to both (Allio et al., 2020), capturing the conjugate heat transfer to the fluid, and (Marek, 2017), modeling the turbulent flow of the coolant. The validated numerical model allows then to assess and quantify the increase of the thermal performance with respect to a plain receiver not equipped with the RR porous matrix.

2. Mock-up and test facility

The Raschig Rings, used as a porous medium in the mockup under consideration in this work, are hollow cylinders, approximately equal in length and diameter, used in large numbers often as a packed bed within columns for distillations or other chemical engineering processes (Sella, 2008). They are usually made of ceramic or metallic material and provide a large surface area within the given volume. In the current work, the RRs are made of copper, coated with a gold alloy and brazed together. The brazing process might modify some RRs thermal properties such as their thermal conductivity, so that the effective conductivity of the porous matrix is unknown. The sketch of the geometry of the single RR adopted here is shown in **Figure 1**. Even if the RR cavity cooling system is patented by Thales, the precise dimension of the rings cannot be disclosed.

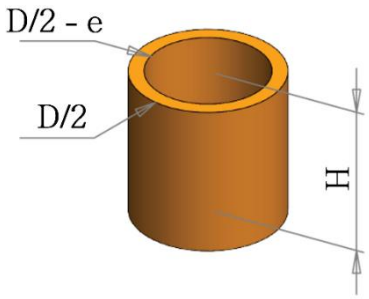

Figure 1 - Schematic view of a single RR: the external diameter D and height H are in the order of few mm, while the thickness e is such to allow making a foil cylinder.

In 2015, a planar mock-up of the gyrotron resonator has been manufactured by Thales Electronic Devices SAS and tested at the Areva Premises under the surface heat load in the range 10 MW/m^2 - 30 MW/m^2, obtained with an electron gun, using subcooled water as cooling fluid. The mock-up is made of two different materials, copper and Glidcop, a family of copper-based metal matrix composite (MMC) alloys mixed primarily with small amounts of aluminum oxide ceramic particles. **Figure 2** shows a schematic representation of the Raschig Rings mock-up and the detail of the

instrumentation that was used to assess the temperature increase (thermocouple insertions below the target area). The mock-up was designed and manufactured to have heat flux focused on the target surface. A collection of pictures, taken in the workshop before the installation of the sample in the solar furnace, are reported in **Figure 3**.

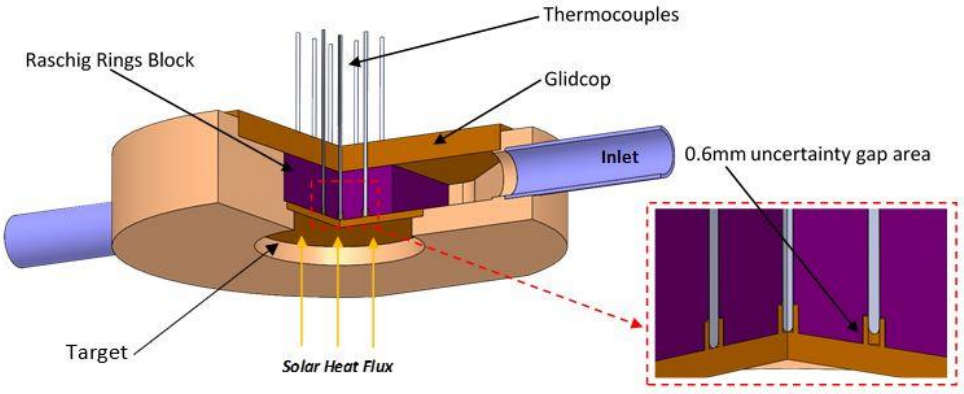

Figure 2 - Schematic view of the RRs planar mock-up: the light-brown volume is made of copper, while the brown one is made of Glidcop. The purple volume represents the portion of the volume filled with Raschig Rings. On the right, a detail of the thermocouples shows the 0.6 mm uncertainty insertion gap space.

The RRs mock-up is equipped with 11 thermocouples (TCs) (**Figure 4**) of the K-type, Class Tolerance I (± 1.5°C in range -40 to 375°C and $0.004 \times |T|$, where T is the measured temperature in Celsius (°C), in the range 375-1000°C). Specifically, it has one TC positioned at the inlet, before the RRs section, one TC located at the outlet into the mixing chamber after the RRs section, i.e. upstream and downstream of the heated zone, respectively, as well as the others 9 TCs which are inserted into the RRs block. For these 9 TCs, installed behind the 2 mm thick target area, see **Figure 4b**, the sensible zone was inserted into dedicated housings, nominally put in contact with the back (wetted) surface of the heated target, with only a gap positioning uncertainty of 0.6 mm, see the inset in **Figure 2**. Therefore, their readings contain some uncertainty as it is not known exactly if each thermocouple measuring tip only touches the copper RRs, the air or both at the same time. A sketch with the reference number for the TCs installed on the sample is reported in **Figure 4a**. Unfortunately, the TC#4 and TC#11 came out broken from the previous experimental campaign at the Areva NP Technical Centre in 2015 and 2016. In addition, two thermocouples of the K-type were placed at the inlet and outlet of the whole mock-up, respectively, to collect a more realistic air bulk temperature upstream and downstream of the mixing chambers, respectively.

Figure 3 - Details of the RRs Mock-up welding to the connection pipes of the solar furnace: (a) before welding, (b) after welding, (c) view of the inside of the two connected pipes.

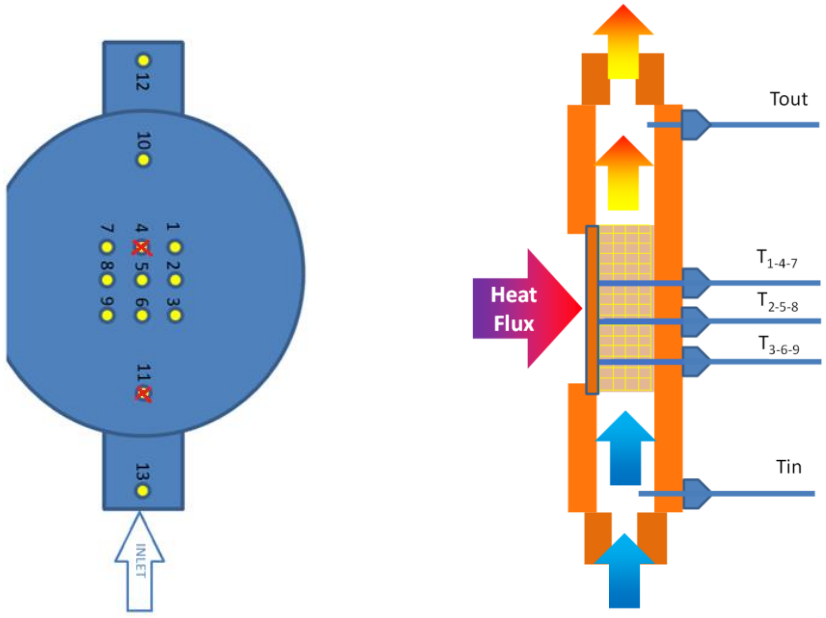

(a) **(b)**

Figure 4 – (a) Sketch map of the thermocouples installed in the sample, with the corresponding identification number; **(**b) longitudinal section of the mock-up, cutting the sample along its axis.

The experimental campaign of the mock-up was carried out in September 2019, financed by the European Union's Horizon 2020 research and innovation program SFERA III, in the 0.6 MW_{th} High-Flux Solar Furnace (SF60) at the Plataforma Solar de Almeria (PSA), which belongs to the Department of Energy of the Centro de Investigaciones Energéticas, Medioambientales y Tecnologicas (CIEMAT), a public research organization under the Spanish Ministry of Economy and Competitiveness (CIEMAT, 2019).

The SF60 operates since 1991, consisting of a 120 m^2 flat heliostat that reflects the solar beam onto a 100 m^2 parabolic concentrator which, in turn, concentrates the incoming rays on the focus of the parabola, where the testbed is placed. A test table movable on three axes is used to place the mock-up with great precision in the focal area. When these components are operating with the shutter fully opened (100%) and a Direct Normal Irradiance (DNI) of 1000 W/(m^2 K), a gaussian shaped solar heat

flux with a peak irradiance at the focus of about 3 MW/m², a total power of 69 kW and a focal diameter of 26.2 cm occur (CIEMAT, 2019). The SF-60 focal diameter is quite higher than the external diameter of the target of the RRs mock-up, which is only 4.5 cm. Since the Raschig Rings block is located only below the target area of the sample to remove the high heat flux, an alumina sheet was put in place to act as a shield for the sample and block part of the concentrated flux reflected by the parabolic concentrator. A hole was made into the Alumina sheet with a diameter of 38 mm, smaller than the target diameter (45 mm), to avoid the solar rays with the highest solid angle with respect to the target area to reach the circular crown of the mock-up instead. **Figure 5a** and **Figure 5b** show a side and front view of the Alumina Shield, while **Figure 5c** shows its back view.

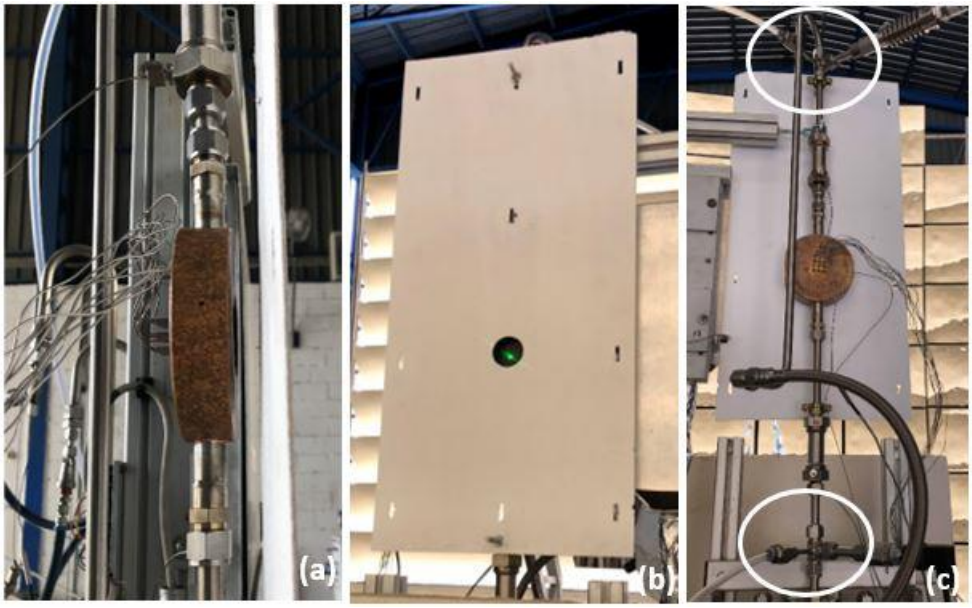

Figure 5 - Alumina shield, (a) side view, (b) frontal view, (c) back view: differential pressure taps positioning.

The final testing circuit, represented in a sketch in **Figure 6**, included primary and secondary loops, with the main following components:

- A 7.5 kW air compressor needed to increase the air pressure of the entire circuit to the value of 10 bar (absolute pressure). The circuit is open, as it sucks air from the ambient;
- A cooler needed to cool down the hot air coming from the primary mock-up test circuit. The cooling working fluid is the water pumped by the pump from the secondary circuit;
- A pump (HP -1) needed to pump the water into the secondary circuit. The pumped water goes into the cooler and into some pipes placed underneath the white table where the radiometer is located, in order to refrigerate it;
- Control valves needed to adjust and control the flow of both air and water into the different pipes;

Beside the thermocouples mounted on the mock-up, the instrumentation installed in the experimental apparatus included:

- A flow-meter needed to check that the air flow-rate during each test remains constant and close enough to the target value. Its nominal accuracy can be split in a baseline component, which is ± 0.1% of the full scale of the instrument (1650 l/m), and in a variable component, equal to ± 0.5% of the actual flowrate reading. Additionally, another ± 0.1% of the full-scale error is to be added due to some uncertainty related to the control stability, plus another ± 5 mbar as the instrument can only read a variation of 10 mbar. In the case of reading for a test duration of few minutes, the uncertainty related to the full scale increases up to 2%, while most accurate measurements require 30 minutes at least;

- A differential pressure drop sensor needed to measure the pressure drop across the RRs Mock-up. A PRE-28 transmitter was used, with an accuracy of ± 0.40% of the actual reading, plus another ± 0.2 %/year instability error, which returns an additional uncertainty of ± 1.4%, as the instrument has been operating for 7 years at the PSA. In addition to this, another ± 0.3 %/10°C should be added to the total error to take into the effect of the warm air, bringing the total value to a global accuracy of ± 2.40%. Note that, starting from the measured pressure drop across the testing section, which includes also the major and minor losses across the piping and connection at both ends of the mockup, see **Figure 5c**, it is possible to compute the experimental "net" pressure drop across the sample;
- A pyrheliometer, for the instantaneous DNI in W/m², needed to check if the operating conditions were suitable (almost constant DNI) to test;

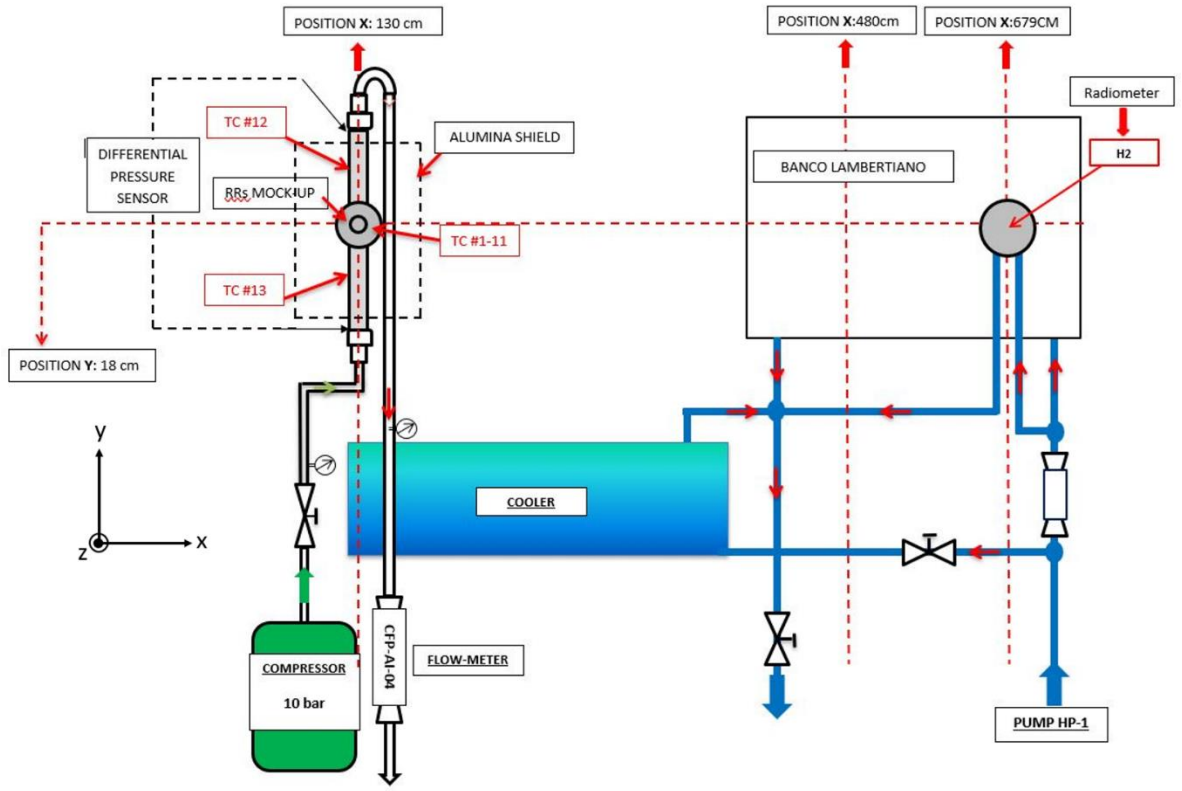

Figure 6 - Sketch of the hydraulic circuit where the sample was inserted for the tests at the PSA.

- A radiometer needed to measure the amplitude of the solar peak flux. To estimate the peak heat flux, the target in the focus of the parabolic collector is moved from the sample to a Lambertian target, through the movement of the mobile testbed. The radiometer adopted at the SF60 has an accuracy of ± 3% (Ballestrin et al., 2003). The incident heat flux, used as boundary condition in the computational model, can be then calculated according to the Gaussian distribution (Roldán and Monterreal, 2014) reported in Eq.(1).

$$\varphi = \varphi_{peak} \cdot e^{-0.5\left[\left(\frac{x}{s_x}\right)^2 - \left(\frac{y}{s_y}\right)^2\right]} \quad (1)$$

where φ_{peak} is the concentrated solar radiation estimated at the focus point (i.e. the peak value) and s_x and s_y are the standard deviations, in x and y direction respectively, both equal to 0.064 (Ballestrin et al., 2003). On top of the given accuracy, other possible sources of inaccuracies may occur: the peak load could change while the measurement panel shifts from the sample to the radiometer, for instance, or the local focus of the flux on the sample could be, instantaneously, in a different position since the heliostat, tracking the sun, is moved by the wind coming from

any possible direction. Unfortunately, it is not possible to quantify this error, which has then been neglected.

3. Test campaign and experimental results

During the two weeks experimental campaign, two different kinds of tests were performed. First, pure hydraulic tests were run by measuring the pressure drop across the sample with different flowrate and, then, thermohydraulic tests were carried out by irradiating the target area of the sample with different heat flux at several flowrates and collecting the readings of the thermocouples in it.

Pure hydraulic tests were performed to investigate the hydraulic properties of the porous media (i.e. the Raschig Rings block) placed below the target area of the sample when using air as a working cooling fluid. The main purpose was to measure the hydraulic characteristic of the mock-up, to provide additional data with respect to those measured on a cylindrical sample in (Allio et al., 2020) for the validation of our computational model. The hydraulic tests have been performed with no heat flux incoming into the target area of the sample (typically during cloudy days), with an inlet pressure of ~10 bar, an air flow rate ranging from 200 Nl/min up to 800 Nl/min and an ambient temperature of about 20°C. After letting the flowmeter running for at least 30 minutes, in order to minimize as much as possible its reading uncertainty, the tests have been performed according to the following guidelines to minimize the experimental uncertainties:

- The duration of the test should be ~ 2 minutes;
- The pressure drop measurements should vary of ± 2.40% + 5 mbar, at maximum;
- The flow-meter readings should vary of ± 2.00%, at maximum.

To process the hydraulic experimental data, a time average of the data measured for each flow rate value has been performed. The total raw averaged pressure drop measurement, reported in **Table 1**, has been offset subtracting the pressure drop deriving from both the minor and major pressure loss of the circuit between the two pressure taps, as sketched in **Figure 7**, evaluated by a simple axisymmetric 2D CFD model. The result is reported in the column "mock-up pressure drop" in **Table 1**, showing that, unfortunately, the largest part of the pressure loss occurs outside of the mock-up, resulting in a poor measurement accuracy, especially at the lowest flow rates.

Table 1 - Summary of the hydraulic tests performed during the experimental campaign.

Test ID	Flow rate	Total pressure drop	Mock-up pressure drop
	[Nl/min]	[$mbar$]	[mbar]
#H1	200 ± 4.3	10 ± 5.2	5.7 ± 5.2
#H2	300 ± 4.8	20 ± 5.5	7.8 ± 5.5
#H3	400 ± 5.3	40 ± 6.0	19.2 ± 6.0
#H4	500 ± 5.8	60 ± 6.4	26.9 ± 6.4
#H5	600 ± 6.3	90 ± 7.2	41.8 ± 7.2
#H6	700 ± 6.8	130 ± 8.1	62.7 ± 8.1
#H7	800 ± 7.3	180 ± 9.3	92.7 ± 9.3

To investigate the thermal properties of the Raschig Rings block, thermal-hydraulic tests were performed in "quasi-steady-state" tests, because of the intrinsic variability of the solar heat source. First, the shutter was regulated to obtain the desired peak heat flux. Then, the mobile test table was moved to place the sample under the focus point. Before the radiometer was positioned a second time under the focus to measure the peak heat flux to compare it with the initial one, to be sure that the heat flux had not varied during the test, the tests were kept running until all the temperature traces got to a quasi-steady state, established based on the following criteria:

- Minimum duration of the quasi-steady state test of 2 minutes;

- Maximum variation of the readings of all the thermocouples within ± 3.00%, as this is the major instrumentation error;
- Maximum variation of the flow-meter reading within ± 2.00%;
- Maximum variation of the peak heat load within ± 3.00% (that translated into a check on the radiometer output before and after the test is performed);
- Check on the wind velocity, which makes the focus position significantly unstable: for safety reasons, the limit provided by the PSA staff of the wind velocity which forced to move back the heliostat in horizontal positions (and therefore to stop any test), was set to the value of 30 km/h.

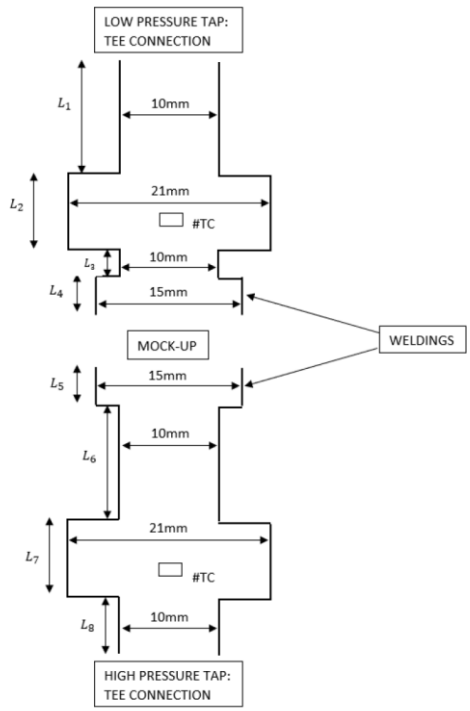

Figure 7 – Sketch of the primary loop connections to the sample, highlighting the main geometrical dimensions relevant for the evaluation of the major and minor losses. For the test of the mock-up: $L_1 = L_6 = 12$ cm, $L_2 = L_7 = 8$ cm, $L_3 = 3$ cm, $L_4 = L_5 = 4$ cm, $L_6 =$ cm.

A summary of all the thermo-hydraulic tests considered in the present analysis, after the above-mentioned checks, is reported in **Table 2**.

Table 2 - Summary of all the thermo-hydraulic tests performed during the experimental campaign.

Date	Test ID	Flow rate	Inlet Pressure	Ambient Temperature	Peak Heat Flux	Shutter Aperture
dd/mm/yy		[l/min]	[bar]	[°C]	$[kW/m^2]$	[%]
13/09/2019	#1-TH1	300 ± 4.8	9.7	20.1 ± 1.5	107 ± 3.2	11.5
13/09/2019	#2-TH1	200 ± 4.3	9.7	21.0 ± 1.5	112 ± 3.4	11.5
16/09/2019	#1-TH2	100 ± 3.8	9.6	22.3 ± 1.5	131 ± 3.9	16.0
16/09/2019	#2-TH2	100 ± 3.8	9.6	27.5 ± 1.5	308 ± 9.2	26.0
16/09/2019	#3-TH2	200 ± 4.3	9.7	27.6 ± 1.5	502 ± 15	32.5
16/09/2019	#5-TH2	100 ± 3.8	9.6	29.1 ± 1.5	500 ± 15	31.0

16/09/2019	#6-TH2	300 ± 4.8	9.7	29.4 ± 1.5	702 ± 21	40.0
17/09/2019	#1-TH3	300 ± 4.8	9.7	25.0 ± 1.5	500 ± 15	25.5
18/09/2019	#2-TH4	300 ± 4.8	9.7	27.0 ± 1.5	298 ± 9.0	21.5
19/09/2019	#1-TH5	200 ± 4.3	9.6	23.6 ± 1.5	299 ± 9.0	24.2
19/09/2019	#2-TH5	200 ± 4.3	9.6	31.1 ± 1.5	727 ± 22	39.4
19/09/2019	#3-TH5	200 ± 4.3	9.6	33.2 ± 1.5	102 ± 3.1	7.00

A summary of the measured temperature increase $\Delta T_{in\text{-}out}$ across the mock-up, for the different flow and heat load conditions, is reported in **Figure 8**, showing that for a given heat load, $\Delta T_{in\text{-}out}$ is inversely proportional to the flow rate, and for a given flow rate $\Delta T_{in\text{-}out}$ is directly proportional to the heat load, as expected. Note that the uncertainty associated with each bar comes from the inaccuracy of the thermocouple (± 1.5°C), plus the standard deviation calculated from the two minutes or more "quasi-steady-state" period needed to validate the test.

When the calorimetry is performed using the measured $\Delta T_{in\text{-}out}$, assuming steady-state condition, the picture represented in **Figure 9** is found: when plotting the absorbed power as a function of the incident power in all cases the thermal efficiency, defined as the ratio between the two quantities, is around 50%. At the lowest flow rate, the efficiency is slightly below 50%, while it is slightly above that value, and comparable within the error-bars for the two highest flow rates. The lower absorbed power for the lowest flow rate can be explained considering that the highest temperature values reached for the lowest flow rate, see **Figure 8**, drives higher losses that, for a given incident power, reduce the absorbed power if compared to the case at highest flow rates.

The overall readings of the thermocouples in the RR block are condensed in **Figure 10** (some of the TC were malfunctioning during certain periods of time, namely TC #6 and TC #8, so that their readout has been omitted when their signal was completely flat). It is clear that the temperature measured by the TC increases along the fluid path due to the heating from the target. Unfortunately, the TC #4, which is the thermocouple located under target downstream, on the symmetry plane, that should correspond to the highest temperature, was broken. Moreover, the expected left-right symmetry in the temperature measurement is only roughly met, but that could be due to the uncertainty in the positioning of the TC heads, see also above.

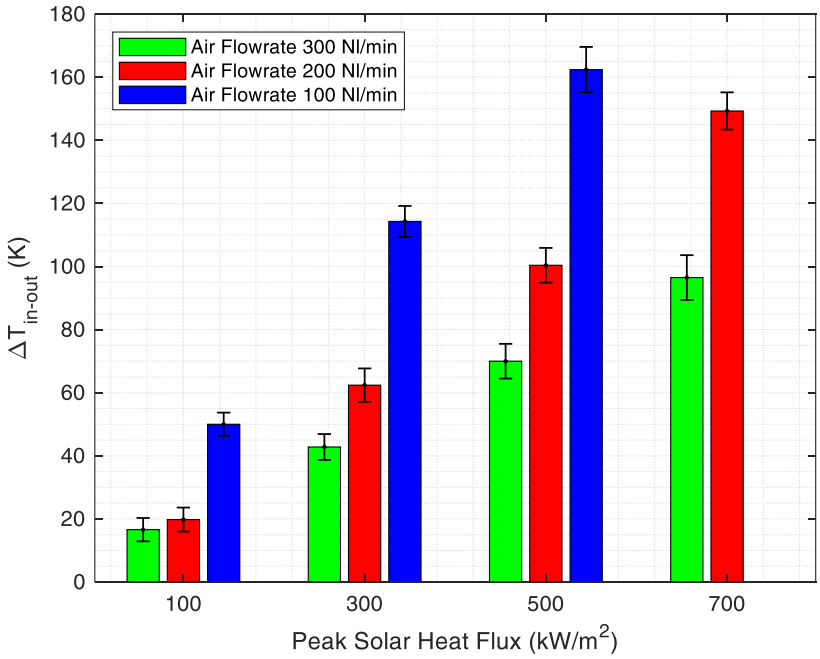

Figure 8 – Temperature difference ($T_{outlet} - T_{inlet}$) measured across the sample at different values of the peak heat flux, for the different tests values of the air flow rates.

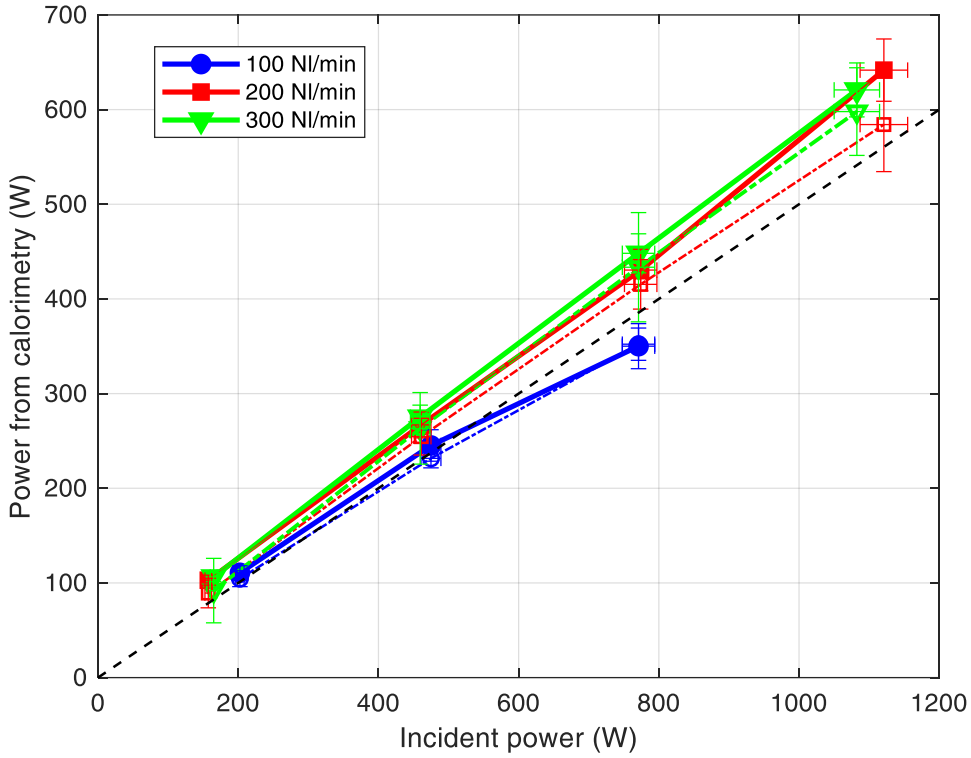

Figure 9 – Power computed by calorimetry as a function of the incident power, for the different tested flow rates: experimental values (solid lines and symbols) and computed values (thin dash-dotted line with open symbols). The dashed line represents the 50% efficiency.

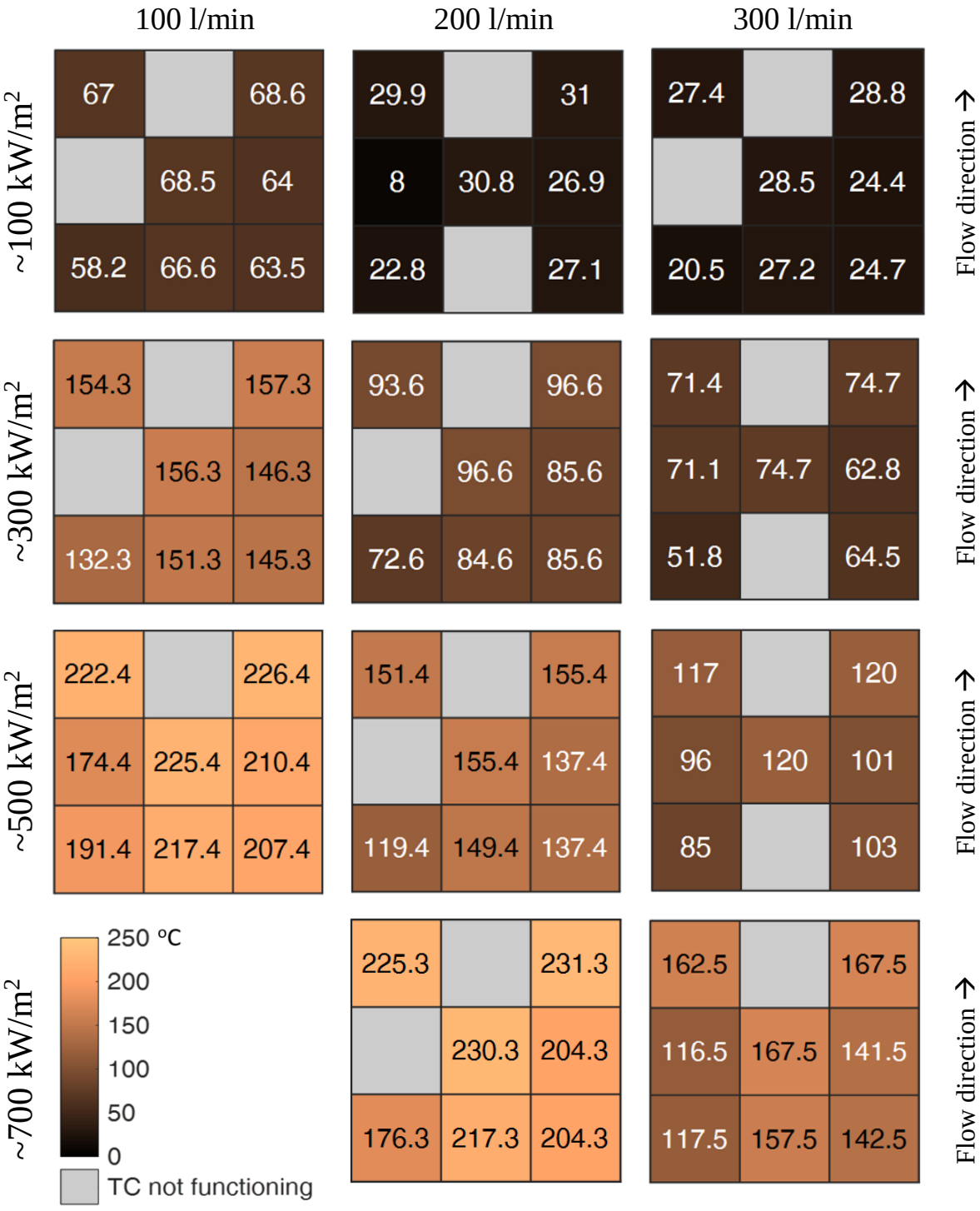

Figure 10 –Temperature increase (with respect to the air inlet conditions) measured in the RR block during the thermal-hydraulic tests in Table 2.

4. Development and validation of a numerical model for the mock-up

4.1. Simulation model and setup

The 3D CFD steady-state conjugate heat transfer problem with a non-uniform heat flux of the mock-up model has been solved with the aid of the commercial software STAR-CCM+ v.10 and v.14 (CD-adapco, 2018).

The geometry used in the simulations is shown in **Figure 11** and will be used for both pure hydraulic and thermohydraulic simulations. Thanks to the symmetry of geometry, boundary conditions and thermal driver, it has been possible to reduce the domain to just half of it, thus significantly reducing the computational cost of each simulation (Bertinetti at al., 2018).

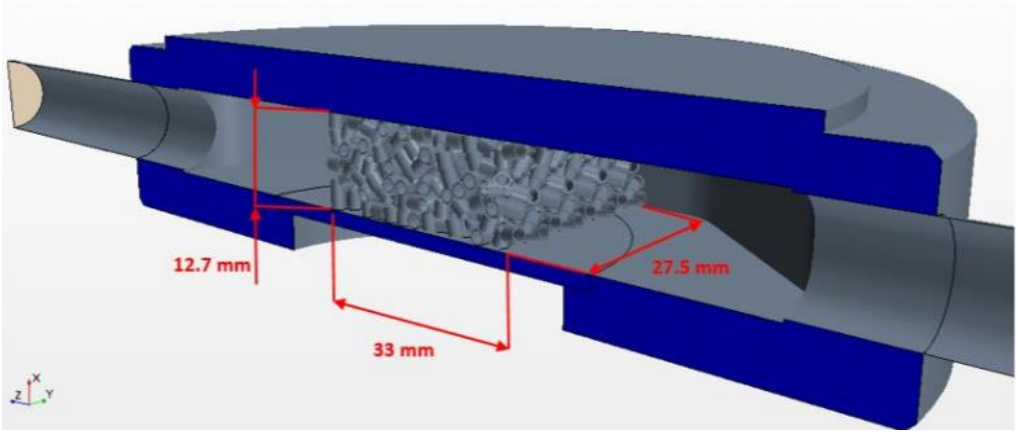

Figure 11 - View of the simulated domain.

The computational domain is subdivided into two regions, one being the solid of the sample (Glidcop) and the other one being the fluid (air). The solid volume of the 11 thermocouples is not included in the simulations.

The driver for the simulations of the thermal-hydraulic tests is the heat flux, having a Gaussian distribution as in Eq. (1), applied to the circular target area (external surface) of the mock-up. The peak flux ranged from 100 kW/m^2 up to 700 kW/m^2, depending on the simulation. The Gaussian function (see Eq. 1) is applied in such a way that the peak of the flux corresponds to the center of the target area, while the minimum value corresponds to the border of the same area. The absorptivity coefficient for the solar radiation α was set to 0.64 (Toolbox, 2019), applied to the target area of the sample, for all the simulations. The surface heat load is then let free to diffuse in the mock-up envelope, as well as in the porous medium.

The fluid boundary conditions for all simulations include the inlet mass flowrate and the inlet air temperature T_{in}, both depending on the test simulated. For the outlet section, a uniform value of the pressure p_{out} was set equal to 10 bar.

The solid boundary conditions for the thermal-hydraulic simulations include thermal losses by free convection and radiation to the environment, applied to every surface facing the open environment. The convective losses are computed according to Newton's cooling law, as a function of the wall surface temperature (computed by CFD), the ambient temperature and the heat transfer coefficient. The ambient temperature was monitored during the test sessions, while the heat transfer coefficient has been estimated using the empirical correlation in Eq. (2) (Incorpera et al, 2006);

$$Nu = \left[0.825 + \frac{0.387 \cdot Ra^{1/6}}{\left[1 + \left({}^{0.492}/_{Pr} \right)^{9/16} \right]^{8/27}} \right]^2 \quad (2)$$

The radiative heat losses computed using an emissivity $\varepsilon = 0.78$ (Toolbox, 2003) are also applied on every dispersing surface.

For the solid region, the steady-state heat conduction equation, with temperature-dependent thermophysical properties, is solved not only for the external envelope of the mock-up but also for each RR. The discrete element model (DEM) approach was adopted to generate the geometry random distribution of rings, as done in previous works on the same topic (Allio et al., 2020), (Savoldi et al., 2018). DEM is typically used for complex modeling of particulate material behavior in chemical, food, metallurgical, mining, and other industries. It is used for instance to simulate deposition of particles under gravity, particles mixing applications, particle-fluid interaction to trace the granular material in a continuous fluid flow. Notwithstanding its great potential, the DEM is also very suited to just generate complex geometrical domains were many particles with the same geometrical characteristics are present, without any particle motion during the simulation of interest. The RR matrix generation procedure consisted of three steps: 1) generation of the volume of the RR matrix, 2) actual DEM simulation, consisting of a time-dependent study in which, at each time step, a certain number of solid cylindrical particles of the same outer size of the RR, were injected into the volume where the porous matrix should be built, 3) replacement of the solid cylinders by the hollow cylinders. The resulting computational domain is shown in **Figure 11**. For the RR matrix, the effective value of the heat conductivity is set to 2600 W/m/K (Bertinetti, 2019), which is quite larger than the Glidcop or copper conductivity, because it accounts for the fact that the contact between the brazed rings is much wider than the contact point present in the model. For the Glidcop density and specific heat, the copper values are adopted. Once the computational domain is built, including the solid volume of the RRs, the conjugate heat transfer problem is solved, simulating not only the solid matrix but also the flow field within them.

As far as the selection of computational models is concerned, for the fluid region, where the air turbulent flow is compressible and all its thermo-physical properties are temperature-dependent, a segregated flow solver was chosen. The flow is in turbulent conditions in the inlet/outlet pipes for all the simulated values of the flow rates, with the value of the Reynolds number (Re) varying between 2.4×10^4 and 1.1×10^5. The flow conditions in the RR region is evaluated looking at the so-called "pellet Reynolds number" Re_P, which is defined using the mean velocity at the inlet of the RR region and the characteristic length computed as the diameter of the sphere equivalent to the volume of a single ring. When $Re_P > 600$ turbulent conditions are met (Allio et al., 2020); in the case at hand, Re_P varies between 600 and 2400.

Following the Reynolds-Averaged Navier-Stokes approach with two-equations to deal with turbulence, the k-ω SST (Menter) turbulence closure (Malalasekera and Versteeg, 2007) was selected here, with an all-y+ wall treatment, as already successfully done in (Allio et al., 2020). It is well known that the k-ε model is unsatisfactory in predicting separating and rotating flows in the near-wall region, resulting in an overestimation of turbulent kinetic energy κ and of the turbulent viscosity; this is mainly due to the empirical nature of the constants used in the equation for the dissipation rate ε (Mohammadi and Pironneau, 1994). On the other hand, the k-ω model has improved performance in modeling the boundary layers under adverse pressure gradients, which is a critical feature of the case under study: indeed, the presence of the RR induces a tortuous flow pattern for the coolant. Our selected turbulence model, the SST-Menter k-ω is able to work as a standard k-ω in the near-wall region, inside the RR block, and as the k-ε model in the main core of the fully turbulent region at the inlet/outlet of the RR block. The energy conservation was also solved with a segregated fluid temperature model.

The mesh for the simulations is a polyhedral cells-based mesh with around 8.9 million of elements. It is built with a general base size of 1.2 mm that has been refined to the value of 0.7 mm for the fluid region and down to the value of 0.2 mm for the portion of the volume that contains the Raschig Rings. A number of 5 prism layers has been chosen for the mesh. This final mesh has been chosen through a grid independence study and a total computational inaccuracy of ~0.5% is obtained with a Richardson extrapolation (Ferziger and Peric, 2002). A selection of the grid independence analysis results is shown in **Figure 12**. The analysis has been performed computing the main thermal and hydraulic quantities of interest using three different meshes. In the abscissa of the plots a normalized cell base size computed using the total number of the cells is reported. A generic view of

the meshed geometry utilized for the simulations is shown in **Figure 13a**, while in **Figure 13b** a detail of the mesh in the RRs region is shown.

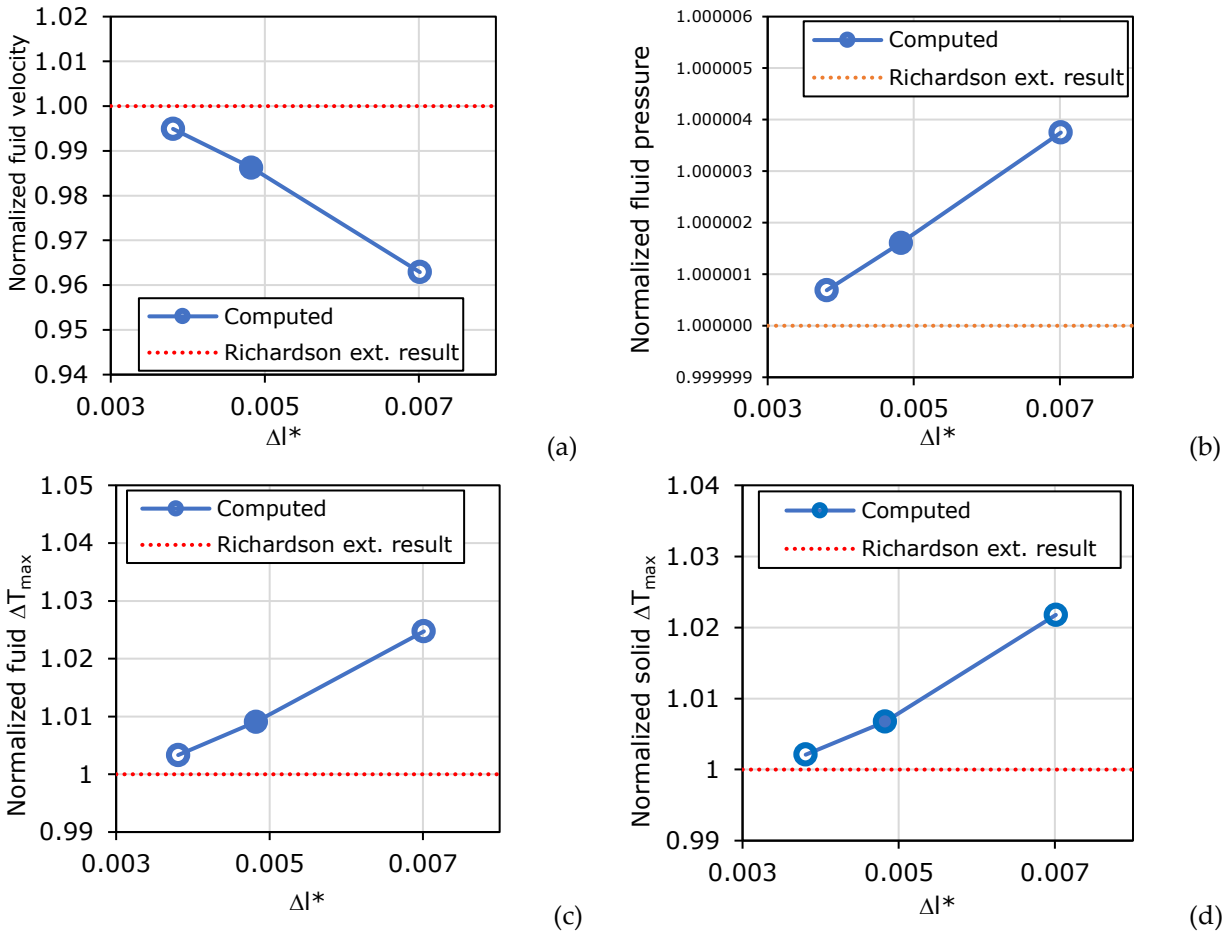

Figure 12 - Grid independence analysis varying the base size of the mesh, for a flow rate of 200 Nl/min and a heat flux of 500 kW/m^2. (a) Mean velocity in the outlet manifold (section at z = 35 mm); (b) pressure in the outlet manifold (section at z = 35 mm); (c) maximum temperature difference of the fluid with respect to the inlet condition; (d) maximum temperature difference of the solid with respect to inlet condition (**d**) All the quantities are normalized to the asymptotic solution evaluated through a Richardson extrapolation. The filled circles highlight the mesh selected for the simulations in the present analysis. $\mathbf{\Delta l}^* = \sqrt[3]{\mathbf{1}/\boldsymbol{N_{cell}}}$ is the normalized base size of the grid cells calculated on the total number of the mesh cells.

The computational cost of the complete model can be subdivided in the cost for the generation of the porous matrix, through the DEM simulation, the cost for the mesh generation and the cost for the actual simulation. The DEM generation weighs about 5% of the total cost, while the mesh generation, particularly challenging in the porous region, weighs 10% of the total. The thermal-hydraulic simulation can be further subdivided into pure hydraulic simulation, which represents about 5% of the total cost and requires about 3000 iterations to achieve convergence of fluid physics, and the conjugate heat transfer simulation, with thermal driver and temperature-dependent material properties, which represents the remaining 80% of the cost and requires about 35000 iterations to achieve a satisfactory convergence.

4.2. Hydraulic characteristic

The accuracy of a similar CFD model in reproducing the pressure drop across a cylindrical mock-up of a gyrotron cavity has been recently demonstrated using water as the process fluid (Allio et al,

2020). The suitability of the numerical model in reproducing the measured pressure drop across the planar mock-up in the case of a compressible fluid (air) is assessed here. Note that also a limited number of pressure drop tests performed on the same sample at the AREVA and THALES premises, respectively, using water as process fluid, were also available to us (Rozier, 2015), so that a comprehensive validation of the numerical model as far as its capability to compute the hydraulic characteristic of the flow through the RR region is possible here, after the detailed analysis of the computed flow and pressure field.

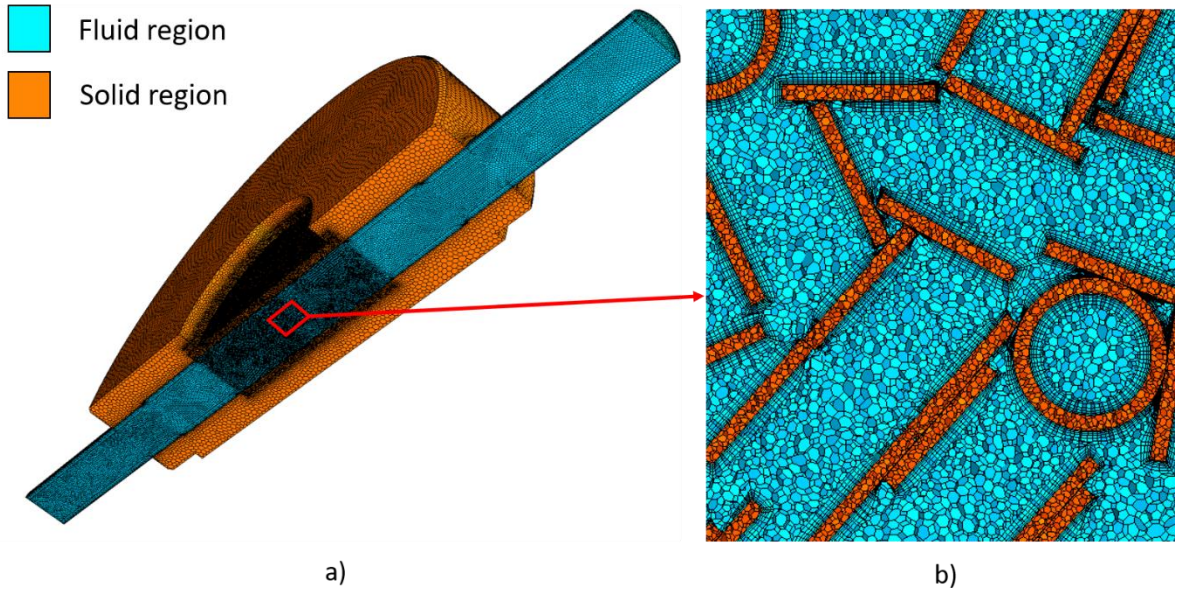

Figure 13 - Mesh view, (a) general view; (b) detail of the mesh in the RRs region.

The analysis of the flow field in random packing structures has been the topic of several experimental and numerical studies, as it has a relevant effect on pressure drop and heat transfer enhancement. The velocity scene is presented in **Figure 14**, showing strong inhomogeneities in both directions and the generation of primary vortices at the end of the inlet pipe. In addition, the detail on the RRs region reveals a dependency of the velocity on the orientation of the RRs: stagnation points occur when the ring is perpendicular to the main flow, while a parallel orientation produces a significant increase in the local velocity.

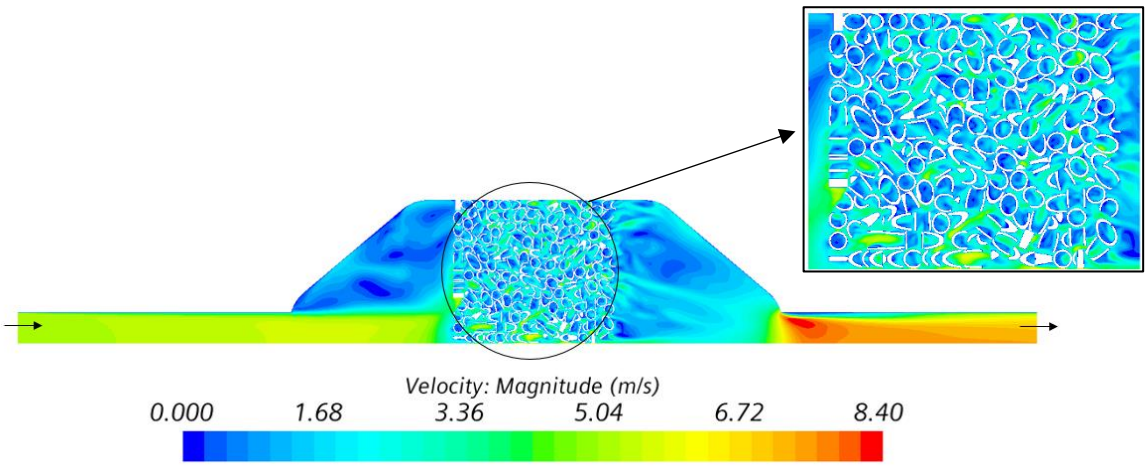

Figure 14 – Computed flow field on the y-z plane passing through the axis of the inlet/outlet pipes, for the simulation at 300 l/min and 500 kW/m^2. Inset: zoom of the flow field in the RR region.

As a consequence of the generation of stagnation points, the number of streamlines that enters the RRs region is higher than the one exiting it, as reported in **Figure 15**, where the streamlines are associated with the scalar velocity. The vortex in the entrance region is highlighted as well. Furthermore, the pattern of the fluid particles appears to be tortuous, increasing the pressure drop across the RRs region. The pressure field in the y-z direction is presented in **Figure 16**, showing the drawback of random packing beds: the pressure decreases as the air flows inside the RRs, for a total drop of approximately 1000 Pa for the flow rate of 300 l/min. The RRs block accounts for 82% of that.

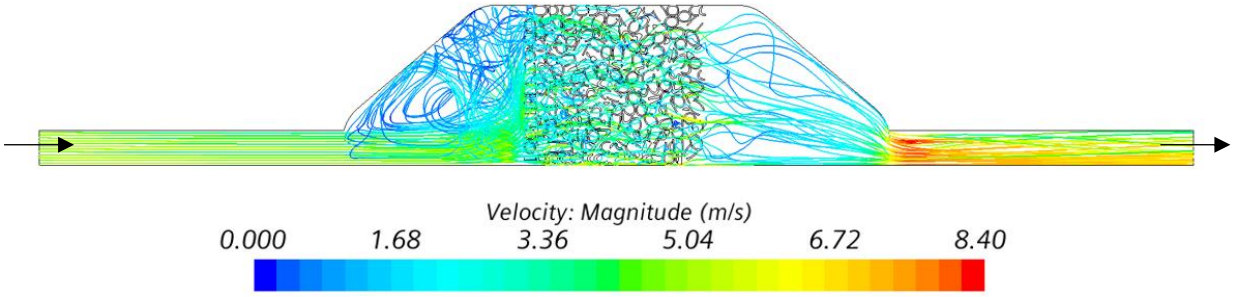

Figure 15 – Computed streamlines of the fluid on the y-z plane passing through the axis of the inlet/outlet pipes, for the simulation at 300 l/min and 500 kW/m².

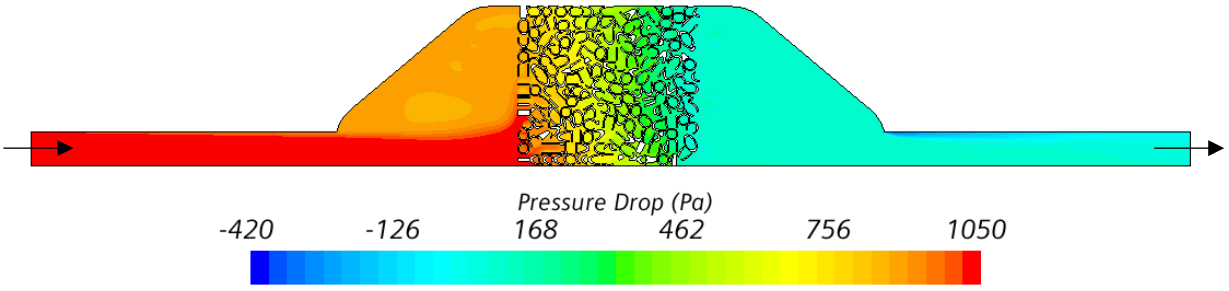

Figure 16 - Computed pressure drop on the y-z plane passing through the axis of the inlet/outlet pipes, for the simulation at 300 l/min and 500 kW/m².

The comparison between the experimental and the computed characteristic, represented in **Figure 17**, shows a very good agreement at mass flow rates below 15 g/s (600 Nl/min), while the computed results tend to underestimate the measurements at the highest values of the measured flow rate. The error-bar attributed to simulated values resulted from the uncertainty on the flow rate, combined with the uncertainty due to the porosity of the RR matrix, as discussed in (Allio et al., 2020), and with the error on the simulated pressure. Note that the quadratic fit in Eq. (3):

$$\Delta p = 0.2351 \cdot \dot{m}^2 + 0.225 \cdot \dot{m} \quad (3)$$

where Δp is the pressure drop along the mock-up in mbar, and $\dot{m}$ is the air mass flow rate, perfectly fits the computed points with $R^2 = 1$. That peculiarity can be qualitatively explained referring to the theory of the porous media (Bejan, 2013), where Darcy's law describes surface drag through a linear dependence of the pressure gradient on the (seepage) velocity through a coefficient that depends on the porous medium permeability. A non-linear (quadratic) term breaks the linear dependence when the form drag due to the solid obstacles in the porous matrix becomes comparable to the surface drag, see Eq. (4).

$$\nabla p = -\frac{\mu}{K} v - c_F K^{-1/2} \rho_f |v| v \quad (4)$$

In Eq (4), ∇p is the pressure gradient, μ and ρ_f are the fluid viscosity and density, respectively, K is the porous medium permeability, c_F is a dimensionless form-drag constant and v is the seepage velocity (i.e., the average velocity taken with respect to a volume of the medium, and not only of the fluid).

However, the portion of the mock-up containing the porous medium is limited in extension, while the rest of it contains plane channels, with a non-negligible contribution to the pressure drop, the quantitative use of Eq. (4) to derive, for instance, the RR permeability and the form coefficient is not straightforward.

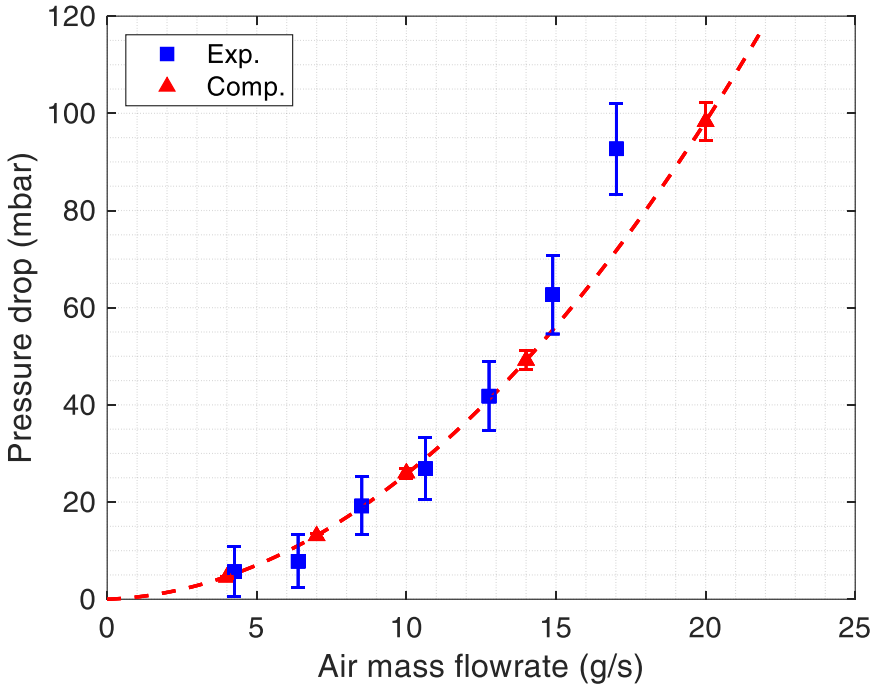

Figure 17 – Hydraulic characteristic of the mock-up: experimental (solid squares) vs. computed (solid triangles). The fit of the computed points is also reported (dashed line).

To investigate further the behavior of the mock-up at high values of the flow rates, where the simulation deviates from the experimental measurements, we should try to take advantage from the pressure drop measurements which have been performed on the same mock-up at the AREVA and THALES premises, respectively, few years ago. Since those tests have been performed using water as process fluid, a dimensional comparison of the hydraulic characteristic of the mock-up in the different tests is meaningless in view of the very different thermophysical properties of the fluid. A fair comparison could be attempted in terms of the dimensionless quantity (Re, f), where Re is the Reynold number and f is the friction factor, but that would require the introduction of a characteristic length (the hydraulic diameter), whose definition is not trivial for the geometry of the mock-up. For this reason, we use here a reformulation of Re and f, already extensively used in other problems (Rizzo et al., 2012),(Rizzo et al, 2013), where the core flow velocity in the standard definition of Re and f have been substituted by the mass flow rate and no geometrical dimensions are involved. The new pseudo-dimensionless quantities Re^* and f^* are defined in Eqs. (5) and (6), respectively.

$$Re^* = \frac{\dot{m}}{\mu} \quad (5)$$

$$f^* = \frac{\Delta p \cdot \rho_f}{\dot{m}} \quad (6)$$

Note that Re^* has the dimensions of a length (m) and f^* those of (m^{-4}). The introduction of $Re^*$and f^*allows the comparison of data obtained using different fluids, without the need of defining a characteristic length. The overall picture of the experimental pseudo-dimensionless pressure drop along with the mock-up, measured in the different experimental campaigns using water and air, is collected in **Figure 18**. Although the error-bar on the water measurement was no available, the comparison between the two different water sets gives an idea of the accuracy of those measurements. The data measured using air show clearly an agreement, within the error bar, with the data measured using water, at least for low Re*. For the two points in air at highest Re*, an increasing trend is shown, which is different from the data measured using water, confirming the odd behavior of the measurement data there, already visible in **Figure 17**. Note that the points computed both using water and air are well in agreement with the measured data points in water at high Re*, and within the error-bar of the measured data points in air at low Re*. Globally, **Figure 18** confirms the suitability of the numerical model developed here to assess the pressure drop of the mock-up equipped with RR. The model, as far as the hydraulic behavior is concerned, might be used with confidence for the design of a porous tubular cavity receiver prototype with RRs used as a heat transfer matrix.

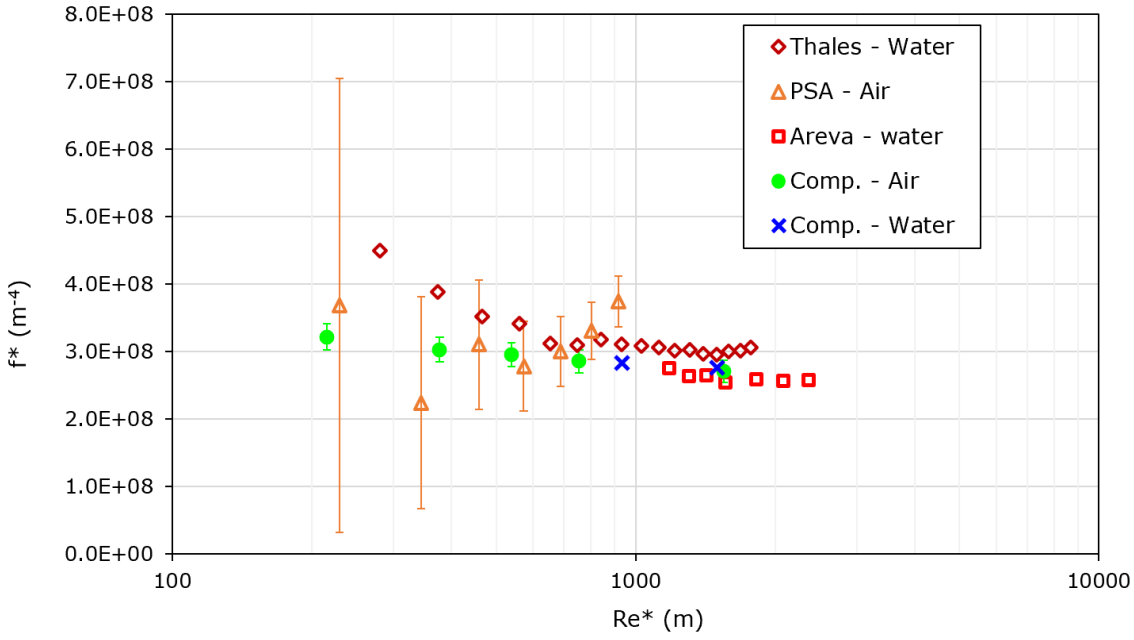

Figure 18 – Pseudo-dimensionless hydraulic characteristic of the mock-up: experimental (open symbols) and computed (solid symbols).

4.3. Simulation of the Thermohydraulic performance

The capability of the numerical model to correctly reproduce the thermal driver of the simulations is first cross-checked through calorimetry, involving the overall temperature increase between inlet and outlet. The computed power entering the mock-up is compared in **Figure 9** to the values obtained, for the different tests, from the measured values, showing a very good agreement at any incident power level and air flowrate.

The total amount of the computed heat losses (both radiative and convective) from the mock-up is reported **Figure 19a**, showing the expected increase with the mean target temperature and the expected decrease with the cooling flow rate, which affects the temperature increase at the target for

a given heat load level, see the labels in **Figure 19a**. According to the computed results, the total losses amount to ~ 10% of the incident power.

The split of the losses between the convective and the radiative contribution is reported in **Figure 19b**, showing that at low temperature the contribution of the two losses is comparable, while the radiative contribution becomes progressively dominant at higher target values, as expected from its non-linear dependence on the temperature difference between the hot and cold surfaces. Note that the losses computed for the simulations at the different flow rates do not overlap, in view of the different temperature distribution on the entire surface of the mock-up, see below, that the average target temperature cannot account for.

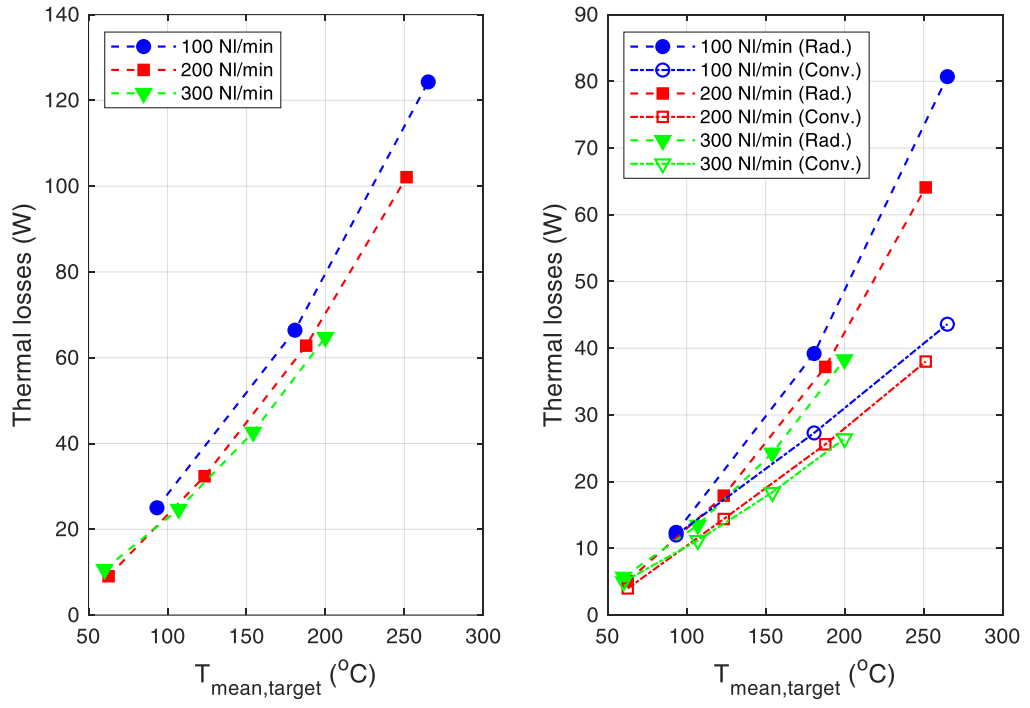

(a) (b)

Figure 19 - Computed thermal losses from the mock-up, as a function of the mean temperature of the target, for the different tested flow rates. (a) Total losses, (b) Radiative and convective losses.

For a single test (300 Nl/min and 500 kW/m²), the computed temperature map in all the solid components of the mock-up is reported in **Figure 20**, showing that the hot spot is not centered in the target but tends to slide downstream because of the direction of the active cooling in the mock-up. The average temperature of the mock-up envelope out of the target region is significantly above the ambient temperature, demonstrating a strong role of parasitic conduction in the metallic structure around the target. Moreover, just one layer of RRs, in direct thermal contact to the target, significantly contributes to the heat removal.

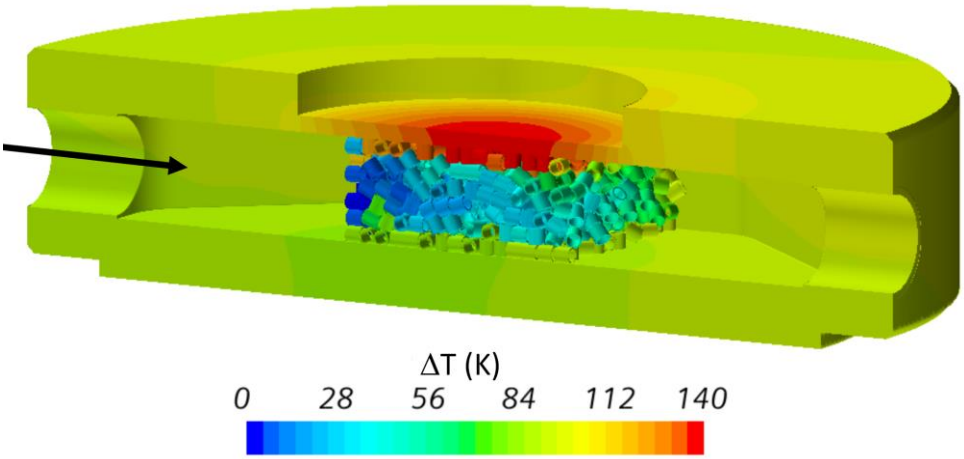

Figure 20 - Computed field of the solid temperature increase with respect to the ambient value on different surfaces, for the case at 300 Nl/min and 500 kW/m².

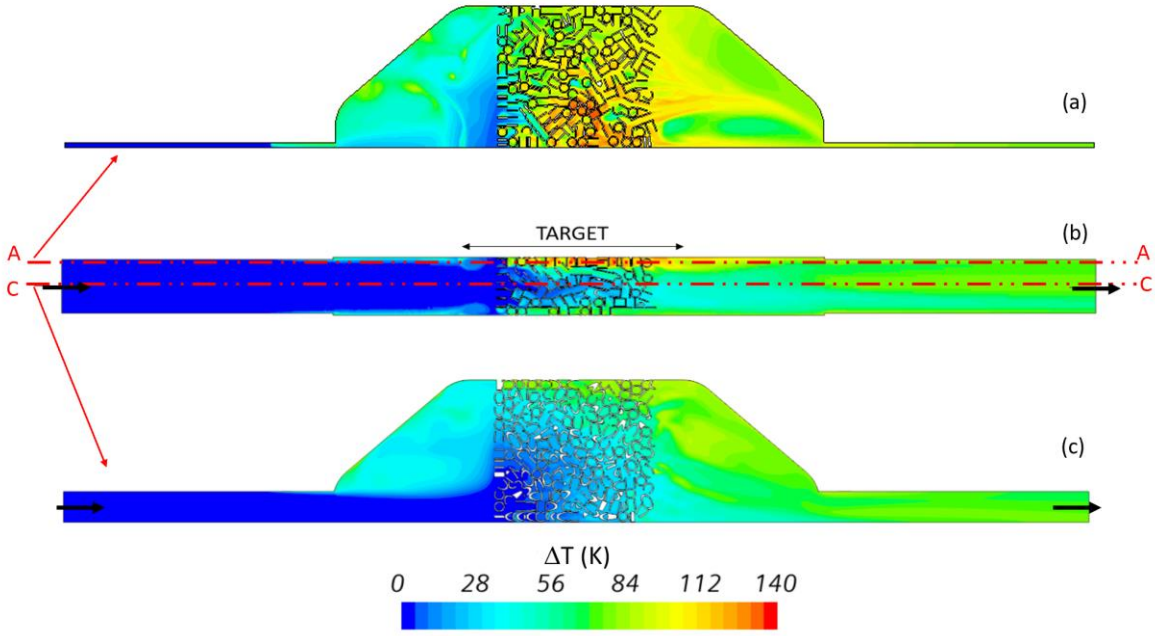

Figure 21 - Computed field of the air temperature increase with respect to the ambient value on different surfaces for the case at 300 Nl/min and 500 kW/m². (a) longitudinal surface (y-z plane) at 3 mm from the target heated surface ,corresponding to the dashed line "AA" in (b); (b) transverse surface (x-z plane) corresponding to the symmetry axis of the sample; (c) longitudinal surface (y-z plane) at 8.5 mm from the target heated surface ,corresponding to the dashed line "CC" in (b).

For the same test case of **Figure 20**, the computed temperature map for the air on different cross-sections of the mock-up is reported in **Figure 21**. From the two longitudinal sections (**Figure 21a,c)**, taken at different depths below the heated surface, it is shown that already in the inlet manifold the air temperature starts to increase due to the parasitic conduction through the structure from the target region. The fresh air flow enters the middle of the RR region (**Figure 21b)**, as a sort of jet from the inlet pipe, while the top (target region) and bottom sides of the mock-up experience a higher coolant temperature in view of the proximity to the wall, which is heated directly or indirectly (parasitic conduction). The longitudinal section closer to the target in **Figure 21a** keeps the memory of the location where the peak incident flux was experienced, while in the longitudinal section far from the target in **Figure 21c** it is shown that the air jet tends to keep the flow colder in the middle of the mock-

up. In both sections, a strong mixing occurs in the outlet manifold, driven by the vortices in the flow field , see **Figure 14** and **Figure 15**.

The validation of the thermal aspects of the CFD simulation is first performed on the entire set of TC measurements for one test at the high heat flux, and the results are reported in **Figure 22**, showing an excellent agreement between the simulations and the experimental data, within the error-bars. The definition of the right error bar is a crucial step in the validation process. The experimental error bar, which was already shown in **Figure 8**, takes into account the ±1.5 K intrinsic reading uncertainty of the thermocouples (which were counted twice since it is a temperature difference between two thermocouples) plus the standard deviation calculated from the two-minutes or more "quasi-steady-state" period needed to validate the test. The computational error bar is less straightforward. It accounts for both the input parameters and mesh independence uncertainties. The input parameters error was considered by solving the thermohydraulic model in the two cases that would have given the maximum and minimum temperature results: maximum heat flux with the minimum flowrate and minimum heat flux with the maximum flowrate, respectively. Once these two simulations were solved for each experimental case, the 0.5% uncertainty related to the mesh independence study was also considered. The overall agreement on the entire set of thermocouples is reasonable, although a large disagreement is found for TK06, at the inlet in the symmetry plane. At the TK06 location, in fact, due to the randomness of the RR displacement in the DEM simulation, there is by chance a poor contact between the RR matrix and the target, see also **Figure 20**, so that the local comparison returns a large underestimation of the measured value. The agreement in the values of TK09-TK03 is good: the computed value falls between the two measured values and it is comparable to both them, within the error-bars. Considering, now, the three thermocouples belonging to the central row, an excellent agreement is computed in the middle, close to the center of the heat load; the agreement on TK02 is within the error bar, while the computed TK08 is largely above the measured values. Note, however, that TK08 could be unreliable as it was not working properly in many of the tests and it is largely below the measured value of TK02. As far as the two sides thermocouples located further downstream below the target, the two measured values are in good agreement and both above the computed one out of the error-bar. A lower computed value can be again due to a local poor thermal contact between the heated target and the rings.

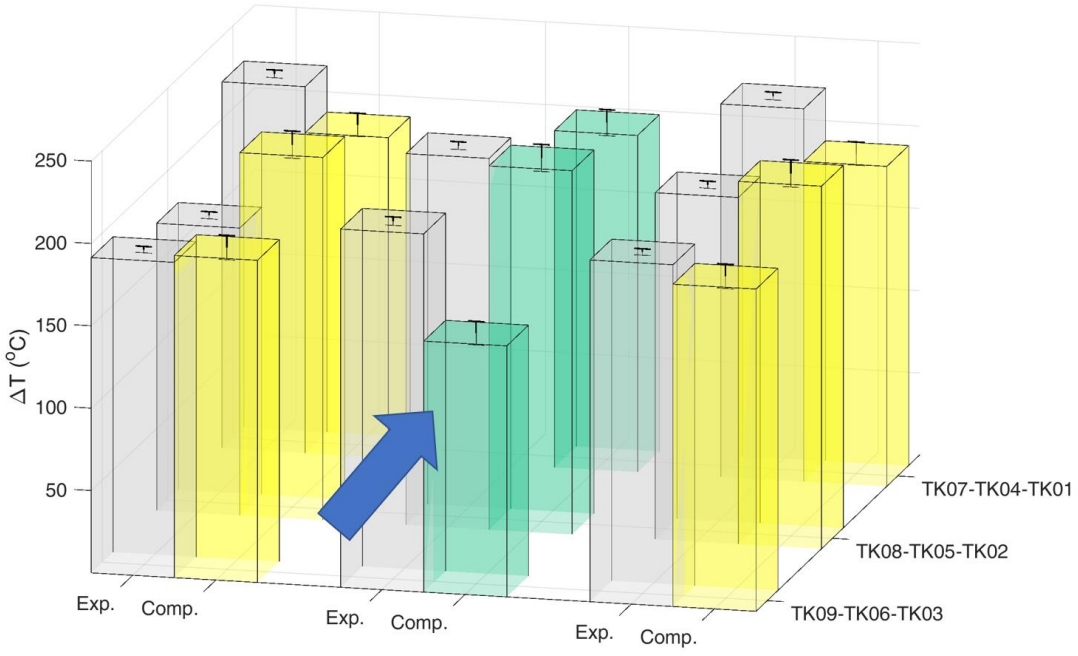

Figure 22 - Comparison between experimental and computed results: case with 700 kW/m² and 300 l/min.

An extensive comparison with the CFD results, including the entire dataset, has been performed on the peak value TK05, as reported in **Figure 23**. A very good match is found between the computed and measured values, for all the cases under exams: flowrate 100-300 Nl/min and peak heat flux 100-700 kW/m^2. The expected trend of temperature increase with the peak heat flux is retrieved, the steeper the slope the lower the mass flow rate is. A parametric analysis performed on the effective conductivity adopted for the RR region has been performed on the test case at the highest load, using the value of 2000 W/m/K, which was the minimum value quoted in (Bertinetti, 2019). The computed results, in that case, showed differences in the order of 0.1K, which can be considered negligible. The tests of the planar mockup with the available diagnostic do not provide useful information for fine tuning of the effective RR conductivity.

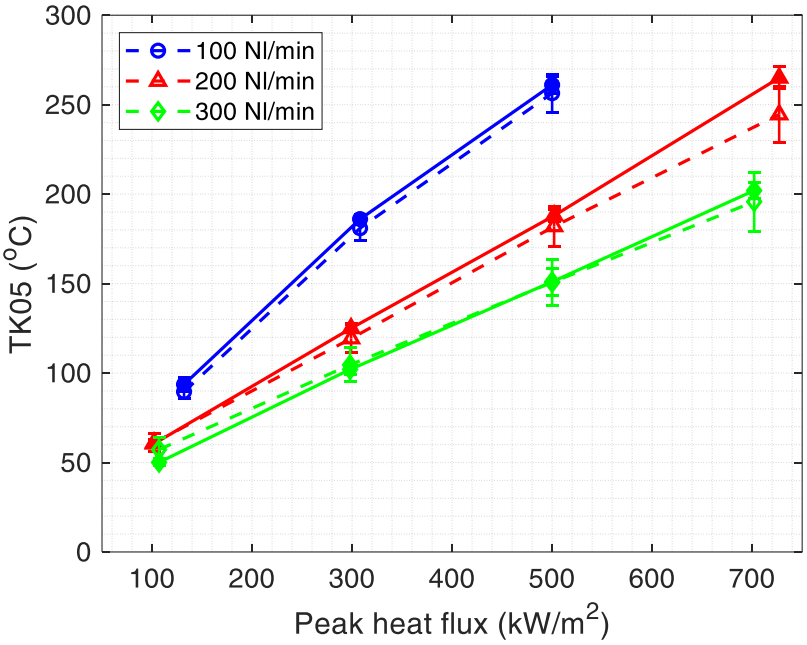

Figure 23 – Validation of TK05 temperature for different flowrates. Computed (solid symbols) vs measured (open symbols), with respective error-bars.

A more detailed investigation of the computed results allowed assessing the hot-spot temperature on the heated surface of the target, reported in **Figure 24**, which could not be measured directly. It was checked that the tests were very far from the melting temperature of the target, i.e. 1083°C (Davis and Smith, 1996), but also from the brazing temperature of the RR, which is 970°C and constitutes an upper bound temperature for the tests. Note that, while for the gyrotron mock-up the thermal stresses are a key issue in guaranteeing the device performance (Leggieri et al., 2020), here the thermo-mechanical constraints are relaxed, since the mock-up is free to expand in the horizontal direction, and just loosely bounded in the vertical direction. The overall picture of the hot-spot temperature is reported in **Figure 24**, showing that it didn't exceed 300 °C in any of the test conditions, with a maximum gradient of ~ 30 K across the target (hot-cold sides) in the most loaded case.

Note that in the 2019 experimental campaign a maximum temperature increase in the mock-up comparable to that already measured during previous tests in water purposely targeted – a second test campaign is planned for the summer 2021 in the framework of another SFERA III project in 2021 (Sanchez, 2020), targeting much higher temperature values. Extrapolating the plotted trend at the highest flowrate, a maximum heat flux up to 3 times larger than the peak value already tested could be tolerated before reaching the temperature upper bound– this information will be useful in the forthcoming re-tests of the mock-up. Looking at the surface temperature maps in the insets in **Figure 24**, it is confirmed that the hot spot does not occur in the center of the target, but slightly downstream, with a clear cooling effect of the fluid along its flow direction.

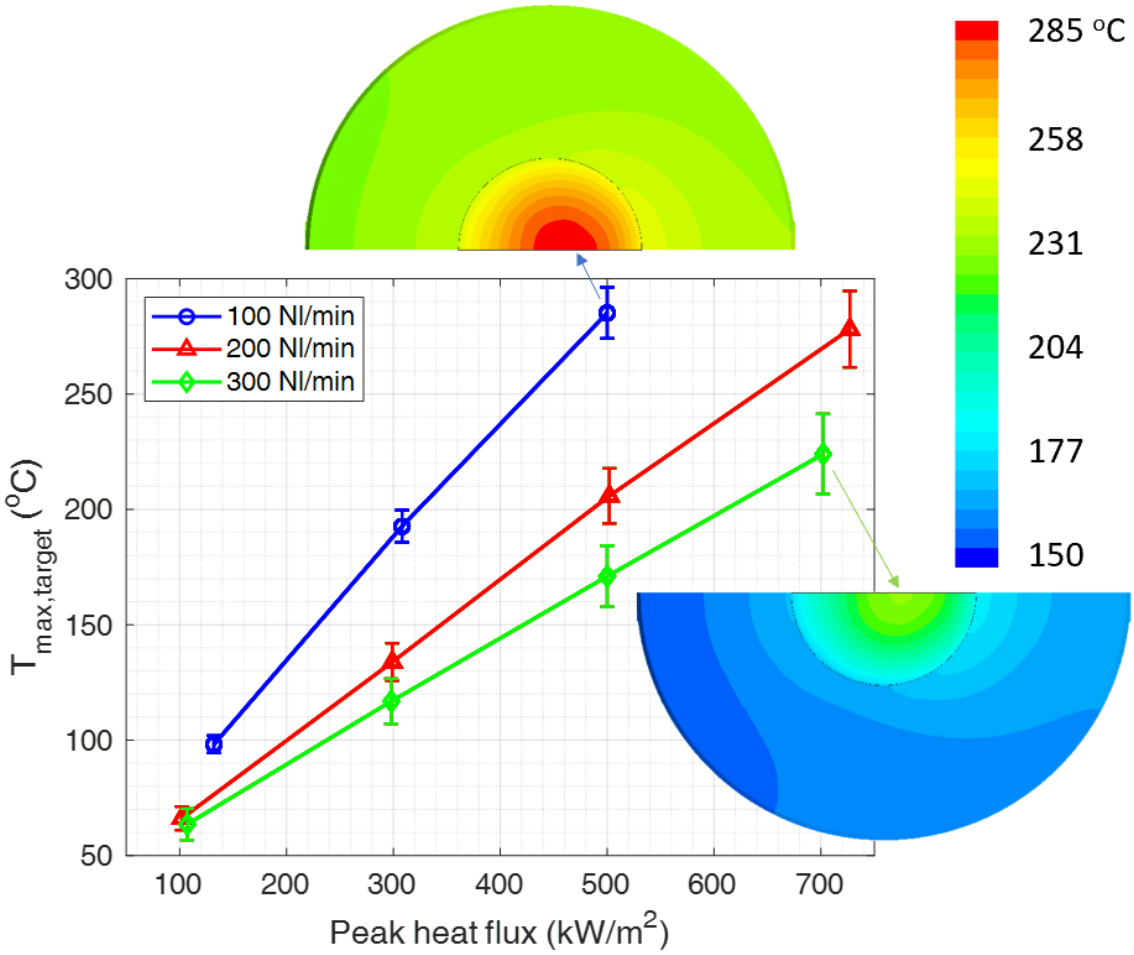

Figure 24 – Computed hot spot temperature on the target as a function of the heat load, for different flow rates. In the insets, the temperature map computed on the heated target and surrounding envelop is also reported for the two cases at 100 Nl/min, 500 kW/m² and 300 Nl/min, 700 kW/m², respectively.

From the computed results, restricting the analysis to the region of the RR, a local heat transfer coefficient HTC, and then local and average pseudo-dimensionless Nusselt number Nu^* could be derived from the definition reported in Eqs. 7-9, respectively:

$$HTC(z) = \frac{\overline{Q_{wall}(z)}}{(\overline{T_{wall}(z)} - T_{bulk}(z))} \tag{7}$$

$$Nu^*(z) = \frac{HTC(z)}{k_f(z)} \tag{8}$$

$$\overline{Nu}^* = \int_0^L Nu^*(z)\,dz = \int_0^L \frac{\overline{Q_{wall}(z)}}{k_f(z) \times (\overline{T_{wall}(z)} - T_{bulk}(z))}\,dz \tag{9}$$

where Q_{wall} (z) is the azimuthally averaged wall heat flux transferred from the wall to the fluid at the axial coordinate z, T_{wall} (z) is the azimuthally averaged wall temperature at the axial coordinate z, T_{bulk} (z) is the bulk air temperature at the axial coordinate z, k_f is the air conductivity, evaluated at the local average wall temperature of the coolant. The resulting HTC ranges from 160 to 400 W/m²/K, depending on the volume flowrate, once the heat flux has been fixed to 500 kW/m², showing a huge enhancement in the heat transfer.

The Performance Evaluation Criteria (PEC) (Wongcharee et al., 2011) can be introduced to summarize the results and to weight the two main phenomena associated to the presence of random

packed beds of RRs: the increase of the heat transfer coefficient and the associated increase of pressure drop (which determines a higher pumping cost). The PEC can be defined as follows:

$$PEC = \frac{\overline{Nu}^* / \overline{Nu}_c^*}{(f^*/f_c^*)^{1/3}} \qquad (Eq.10)$$

Where, the subscript "c" represents clear receiver tube without porous medium and f^* is a pseudo-dimensionless friction factor evaluated through the Darcy relation (Eq. 11):

$$f^* = 2\frac{\Delta p}{\rho \bar{v}^2} \qquad (Eq.11)$$

In Eq.(11), Δp is the computed pressure drop along the mock-up w/o the RRs, $\bar{v}$ is the average fluid velocity between inlet outlet sections and ϱ is the fluid density evaluated at the average bulk temperature along the tube. The values of the PEC as a function of the Re number are reported in **Figure 25**, showing that, when the flowrate increase, the weight of the pressure drop becomes more and more evident. The advantage of the insert of the RRs packed bed is, however, achieved for all the cases, with a PEC between 2 and 2.5. An increase of 50%, on average, is obtained with respect to the porous media configurations studied in (Zheng et al, 2017).

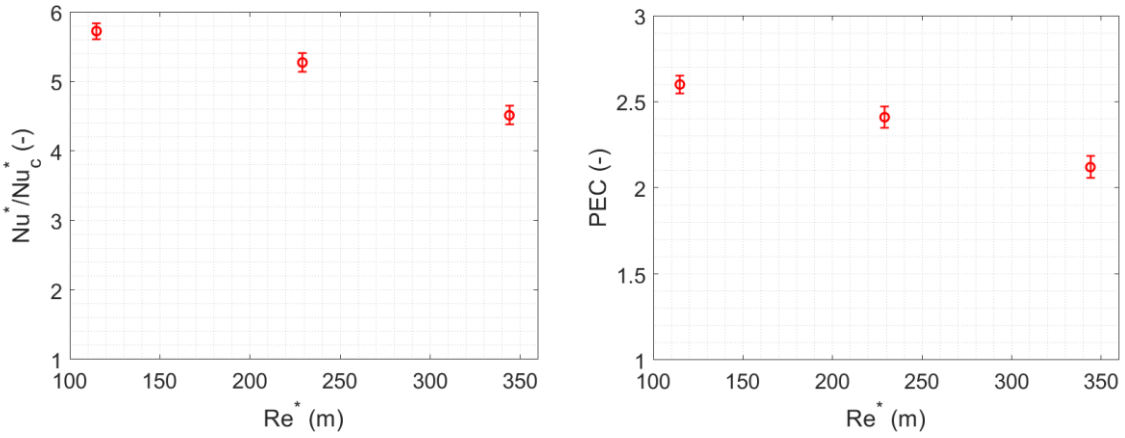

(a) (b)

Figure 25 – (a) Ratio between the computed average Nu* for the mock-up with RRs and for the clear configuration at 500 kW/m^2, as a function of Re*; (b) Computed PEC at 500 kW/m^2 as a function of Re*.

5. Conclusions and Perspectives

A porous receiver, constituted by a rectangular-shaped channel equipped with a Raschig Rings block below the heated side, has been tested for the first time in the solar field, in the furnace SF60 at the PSA, targeting a possible application for Central Towers. The receiver was a planar mock-up of a gyrotron cavity used in nuclear fusion applications, for which the removal of high heat fluxes on a small surface is also a crucial issue. While in the nuclear applications the cooling fluid which flows through the porous matrix is subcooled water, the PSA tests were carried out using ambient air as the operating fluid.

The tests allowed measuring the hydraulic characteristic of the sample and its thermal response when subject to different heat load levels and cooled by different air flowrates.

The development of a suitable numerical thermal-hydraulic model, based on the DEM technique as far as the RRs generation is concerned, allowed, after a comprehensive validation against the measured hydraulic and thermal-hydraulic data, to analyze the test results. The radiative and convective losses turned out to be ~ 10% of the incident power. The maximum temperature reached

on the heater target stayed in all cases below 300 °C in the 2019 test campaign, with a maximum difference of 30 K across the target. That leaves space to increase significantly the heat load in the future tests, planned at the PSA in July 2021, to check the actual operating limits of such a target.

The numerical model allowed also to quantify the effectiveness of introducing the porous matrix below the heated target, with respect to a plane rectangular channel. The figures of merit of the receiver equipped with RR are very encouraging for the future further development of tubular receivers with that porous matrix. An enhancement in the Nu number of ~ 5 was in fact computed, together with a Performance Evaluation Criteria, combining heat transfer enhancement and pressure drop increase, larger than 2 for all flow rates.

In perspective, from the experimental point of view, a retest the receiver at the PSA is planned for 2021 at large heat loads, to fully explore the operation limits of the sample configuration, targeting an upper value of ~950 °C on the heated surface. From the numerical point of view, with the validated model, we plan to perform a detailed analysis for a tubular receiver equipped with RRs, to check if the enhanced performance of the sample presented here holds for a tubular sample. Also, the optimal dimension of RR will be addressed parametrically both experimentally and numerically, together with a partial filling of the tubes, to identify the best configuration for a high-efficiency air receiver.

Acknowledgements:

The tests have been financed by the European Union's Horizon 2020 research and innovation program: Solar Facilities for the European Research Area – Third Phase (SFERA III) under grant agreement N. 823802. We thank Dr. M. Cagnoli, Dr. R. Bonifetto and Prof. R. Zanino for preliminary discussion on the test campaign. We also thank Dr. A. Leggieri for the careful check that no confidential data owned by THALES, were reported in the paper, and for giving access to the mock-up experimental data collected in previous test campaigns.

We acknowledge the use of the computational resources provided by hpc@polito, which is a project of Academic Computing within the Department of Control and Computer Engineering at the Politecnico di Torino (http://hpc.polito.it).

Abbreviations

CFD	Computational Fluid Dynamics
CIEMAT	Centro de Investigaciones Energéticas, Medioambientales y Tecnológicas
CSP	Concentrating Solar Power
DEM	Discrete Element Method
DNI	Direct Normal Irradiance
ERT	Enhanced Receiver Tube
GCI	Grid Convergence Index
MMC	Metal Matrix Composite
HiTRec	High Temperature Receiver
PEC	Performance Evaluation Criteria
PSA	Plataforma Solar de Almería
RANS	Reynolds-averaged Navier–Stokes
RBD	Rigid Body Dynamics
RRs	Raschig Rings
SF	Solar Furnace
SFERA	Solar Facilities for the European Research Area
SST	Shear Stress Transport
TC	Thermocouple

Greek symbols

α	absorptivity
Δp	pressure drop (Pa)
∇p	pressure gradient (Pa/m)
ΔT	temperature difference (K)
ε	emissivity
κ	turbulent kinetic energy (m2/s2)
μ	dynamic viscosity (Pa·s)
ϱ	density (kg/m3)
Φ	applied heat flux (W/m2)
ω	specific dissipation rate of the turbulent kinetic energy (s-1)

Symbols

c_F	Dimensionless form-drag constant
D	diameter (m)
Dl*	normalized base size of the grid cells
f	friction factor
f*	Pseudo-dimensionless friction factor
H	height (m)
HTC	heat Transfer Coefficient (W/m2/K)
k	thermal conductivity (W/m/K)
K	porous media permeability (m2)
L	length (m)
$\dot{m}$	mass flowrate (kg/s)
Ncells	number of cells
Nl	Normal litre (normal conditions T = 0 °C and p = 1 bar)
Nu	Nusselt number
Nu*	Pseudo-dimensionless Nusselt number
p	pressure (Pa)
Pr	Prandtl number
Q	heat flux exchanged between interfaces (W/m2)
Ra	Rayleigh number
Re	Reynolds number
Re*	Pseudo-dimensionless Reynolds number
s	standard deviation
T	temperature (K)
v	velocity (m/s)
x, y, z	coordinate system

Subscripts

bulk	bulk
c	clear receiver
f	fluid
in	inlet
in-out	difference between inlet and outlet
out	outlet
p	pellet
peak	peak
wall	wall

References

Alkam, M.K., Al-Nimr, M., 1997. Unsteady non-darcian forced convection analysis in an annulus partially filled with a porous material. Journal of Heat Transfer, vol. 119, no. 799-804.

Alkam, M.K., Al-Nimr M.A., 1999. Improving the performance of double-pipe heat exchangers by using porous substrates. International Journal of Heat and Mass Transfer, vol. 42, no. 3609-3618.

Allio, A., Difonzo, R., Leggieri, A., Legrand, F., Marchesin, R., and Savoldi, L., 2020. Test and Modeling of the Hydraulic Performance of High-Efficiency Cooling Configurations for Gyrotron Resonance Cavities. Energies, vol. 13, no. 1163.

Ballestrin, J; Ulmer, S.; Morales, A.; Barnes, A.; Langley, L; Rodriguez, M. "Systematic Error in the measurement of ery high solar irradiance". *Solar Energy material and solar cells., vol. 80*, no. 3, pp. 375-381, 2003.

Becker, M., Fend, T., Hoffschmidt, B., Pitz-Paal, R., Reutter, O., Stamatov, V., Trimis, D., 2006 Theoretical and numerical investigation of flow stability in porous materials applied as volumetric solar receivers. Solar energy, vol. 80(10), no. 1241-1248.

Bejan, A., 2013. Convection Heat Transfer, Fourth Edition, John Wiley & Sons, Inc., Hoboken, New Jersey.

Albajar, F., Cau, F., Leggieri, A., Legrand, F., Perial, E., Ritz, G., Savoldi, L., Zanino, R., Zappatore, A., 2018. Design, test and analysis of a gyrotron cavity mock-up cooled using mini channels. IEEE Transactions on Plasma Science.

Bertinetti, A., 2019. Development of the Multi-physiCs tool for the integrated simulation of the Cavity and its application for the design of gyrotron cavities for thermonuclear applications. PhD thesis, Politecnico di Torino.

Cagnoli, M., Savoldi L., Zanino, R.; Zaversky, F., 2017. Coupled optical and CFD parametric analysis of an open volumetric air receiver of honeycomb type for central tower CSP plants. Solar Energy, vol. 155, 523-536.

Cantone, M., Cagnoli, M., Savoldi, L., 2020. One-side heating test and modeling of tubular receivers equipped with turbulence promoters for solar tower applications. To appear in Applied Energy.

CD-adapco, 2018. STAR CCM+ User Guide Version 13.02.

CIEMAT, 2019, Plataforma Solar de Almeria, Annual Report 2019, available at https://www.psa.es/en/techrep/2019/AnnualReport2019.pdf (last visited on July 2020).

Conroy, T., Collins, M.N., Grimes, R.,2019. A review of steady-state thermal and mechanical modelling on tubular solar receivers. Renewable and Sustainable Energy Reviews, 119:109591.

Davis, P., Smith, J.V., 1996. ITER material properties handbook. J. Nucl. Mater.

Dong, Y., Sosna, B., Korup, O., Rosowski, F., Horn, R., 2017. Investigation of radial heat transfer in a fixed-bed reactor: CFD simulations and profile measurements. Chemical Engineering Journal vol. 317, 204-214.

European Commission, 2011. Final report - SOLHYCO (Solar-Hybrid Power and Cogeneration Plants)., Available online at https://cordis.europa.eu/project/id/19830/reporting/it (last visited in July 2020).

European Commission, 2019. Strategic energy technologies information system: Concentrated solar power. Available online: https://setis.ec.europa.eu/technologies/concentrated-solar-energy (last visited in July 2020).

Ferziger J. H., Peric, M., 2002. Computational Methods for Fluid Dynamics, 4th edition, Springer.

Ho, Clifford K.C., Romano, D., Yellowhair, J., Siegel, N.; Savoldi, L, Zanino, R., 2017. Characterization of particle flow in a free-falling solar particle receiver. Journal of Solar Energy Engineering, 139(2).

Hoffschmidt, B., Pitz-Paal R., Bohmer, R., Fend, T., Rietbrock, P., 1999. 200 kWth open volumetric air receiver (HiTRec) of DLR reached 1000 °C average outlet temperature at PSA. Journal of Physics, IV France 9.

Hoffschmidt, B., Tellez, F.M., Valverde, A., Fernandez, J., Fernandez, V., 2003. Performance evaluation of the 200-kWth HiTRec-II open volumetric air receiver". Journal of Solar Energy Engineering, vol.125, 87-94.

Kumar, K. R., Reddy, K. S., 2009. Thermal analysis of solar parabolic trough with porous disc receiver. Applied Energy, vol.86(9), 1804-1812.

Incropera, F. P., Dewitt, D. P., Bergman, T. L., Lavine, A. S., 2006. Fundamentals of Heat and Mass Transfer. John Wiley & Sons Inc, New York.

Leggieri, A., Bariou, D., Hermann, V., Legrand, F., Lietaer, G., Albajar, F., Sanchez, F., Alberti. S., Hogge, J.-P., Allio, A., Difonzo, R., Savoldi, L., Bruschi, A., Bin, W., Chelis, I., Tigelis, I., Avramidis, K. A., Dammertz, G., Gantenbein, G., Illy, S., Ionnidis, Z., Jelonnek, J., Jin, J., Pagonakis, I. Gr., Rzesnicki, T., Thumm, M., 2020. Upgrade of the European ITER 170 GHz 1 MW CW Industrial Gyrotron (TH1509), In Procedings of 7th ITG International Vacuum Electronics Workshop (IVEW), Bad Honnef.

Lim, S., Kang, Y., Lee, H., Shin, S., 2014. Design optimization of a tubular solar receiver with a porous medium. Applied thermal engineering, vol.62(2), 566-572.

Malalasekera, W., Versteeg, H. K., 2007. An introduction to computational fluid dynamics. The finite volume method, Harlow: Prentice Hall.

Marek, M., 2017. Numerical simulation of a gas flow in a real geometry of random packed bed of Raschig rings. Chemical Engineering Science, vol. 161, 382-393.

Moghaddam, E. M., Foumeny, E. A., Stankiewicz, A. I., Padding, J. T., 2020. Hydrodynamics of narrow-tube fixed bed reactors filled with Raschig rings. Chemical Engineering Science, vol. X, 5:100057.

Mohamad, A., 2003. Heat transfer enhancements in heat exchangers fitted with porous media part I: constant wall temperature. International Journal of Thermal Sciences, vol. 42, 385-395.

Mohammadi, O., Pironneau, B., 1994. Analysis of the k-eps turbulence model. Wiley.

Mwesigye, A., Bello-Ochende, T., Meyer, J. P., 2014. Heat transfer and thermodynamic performance of a parabolic trough receiver with centrally placed perforated plate inserts. Applied energy, vol.136, 989-1003.

Rizzo, E., Heller, R., Richard, L.S., Zanino, R., 2012. Analysis and performance assessment for a 68 kA HTS current lead heat exchanger. IEEE transactions on applied superconductivity, vol.22(3).

Rizzo, E., Heller, R., Richard, L.S., Zanino, R., 2013. Computational thermal-fluid dynamics analysis of the laminar flow regime in the meander flow geometry characterizing the heat exchanger used in high temperature superconducting current leads. Fusion Engineering and Design, vol.88(11), 2749-2756.

Roldán, M. I., Monterreal, R., 2014. Heat flux and temperature prediction on a volumetric receiver installed in a solar furnace. Applied energy, vol. 120, 65–67.

Rozier, Y., 2015. Report on thermal cavity mock-up experiments, Thales Electron Device, Contract ref: F4E-OPE-447, deliverable D3. Available upon request.

Sanchez, R., May 2020. Private communication.

Savoldi, L., Albajar, F., Alberti, S., Avramidis, B.A., Bertinetti, A., Cau, F., Cismondi, F., Gantenbein, G., Hogge, J.P., Ioannidis, Z.C., 2018. Assessment and optimization of the cavity thermal performance for the European continuous wave gyrotrons. In Proceedings of the 27th IAEA Fusion Energy Conference (FEC 2018), Gandhinagar, Indien, 22–27.

Sella, A., Raschig's Rings, vol. 5, Chemistry World, 2008.

Skocypec, R.D., Boehm, R.F., Chavez, J.M., 1989. Heat transfer modeling of the IEA/SSPS volumetric receiver. J. Sol. Energy Eng., vol. 111, 138-143.

Toolbox, 2003. Available online: https://www.engineeringtoolbox.com/emissivity-coefficients-d_447.html. (last visited in July 2020).

Toolbox, 2009. Available online: https://www.engineeringtoolbox.com/solar-radiation-absorbed-materials-d_1568.html (last visited in July 2020).

Uhlig, R., Gobereit, B., Rheinländer, J., 2015. Advancing tube receiver performance by using corrugated tubes. Energy Procedia; vol. 69, 563-572.

Wongcharee K., Changcharoen W., Eiamsa-Ard S., 2011. Numerical investigation of flow friction and heat transfer in a channel with various shaped ribs mounted on two opposite ribbed walls. International Journal of Chemical Reactor Engineering, vol. 9(1).

Wu, Z., Caliot, C., Bai, F., Flamant, G., Wang, Z., Zhang, J., Tian, C.,2010. Experimental and numerical studies of the pressure drop in ceramic foams for volumetric solar receiver applications. Applied Energy, vol. 87(2), 504-513.

Yang, M., Yang, X., Yang, X., Ding, J., 2010. Heat transfer enhancement and performance of the molten salt receiver of a solar power tower. Applied Energy, vol. 87(9), 2808-2811.

Zanino, R., Romano, C.K., Savoldi, L., 2016. Preliminary discrete element modeling of a falling particle curtain for CSP central tower receivers. In AIP Conference Proceedings, vol. 1734. No. 1. AIP Publishing LLC.

Zheng, Z.J., Li, M.J., He, Y.L., 2017. Thermal analysis of solar central receiver tube with porous inserts and non-uniform heat flux. Applied Energy, vol.185, 1152-1161.

Zhu, Q., Xuan,Y., 2018. Performance analysis of a volumetric receiver composed of packed shaped particles with spectrally dependent emissivity. International Journal of Heat and Mass Transfer, vol.122, 421-431.